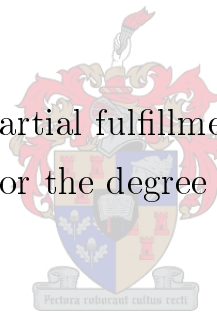# Ultrashort Optical Pulse Characterization

by

Gurthwin Wendell Bosman

Thesis presented in partial fulfillment of the requirements
for the degree of

Master of Science

at the University of Stellenbosch

Supervisor: Prof. E. G. Rohwer
Co-supervisor: Prof. H. M. von Bergmann

March 2008

Declaration

By submitting this thesis electronically, I declare that the entirety of the work contained therein is my own, original work, that I am the owner of the copyright thereof (unless to the extent explicitly otherwise stated) and that I have not previously in its entirety or in part submitted it for obtaining any qualification.

....
Date

Abstract

Various autocorrelation techniques are employed to characterize ultrashort laser pulses in both the temporal and spectral domain. These techniques are; interference autocorrelation (IAC), modified spectrum autointerferometric correlation (MOSAIC), background-free autocorrelation (BFA) and frequency resolved optical gating (FROG). All of these techniques are based on the interaction of a pulse with a time delayed copy of itself within a $\chi^{(2)}$ medium.

Experimental setups for BFA and FROG experiments are developed, which exploit the phenomenon of second harmonic generation (SHG). An existing IAC setup is used for temporal pulse characterization. MOSAIC results are obtained through applying a specific Fourier filter to the IAC data.

IAC and MOSAIC measurements performed on a commercially available femtosecond laser, indicate that the emitted pulse has a pulse duration less than 150 fs and possesses positive linear chirp. BFA and FROG measurements carried out on the same laser system mirror these results.

Pulses emitted by a 20 Hz chirped pulse amplifier are characterized through BFA and FROG. BFA results suggest that the pulse from the amplifier is actually a double pulse. FROG results indicate that the pulse is highly chirped.

The experiments and physical interpretations presented in this work demonstrate the preferred methods of optical pulse characterization for ultrashort laser pulses.

Opsomming

Verskeie outokorrelasie tegnieke is aangewend om ultrakort optiese laser pulse te karakteriseer. Die karakterisering word in beide die tyd en die frekwensie ruimte gedoen. Die tegnieke sluit in; interferensie outokorrelasie (IOK), spektrum gemodifiseerde interferensie outokorrelasie (SGIOK), agtergrondlose outokorrelasie (ALO) en frekwensie opgeloste optiese hekking (FOOH). Hierdie tegnieke word almal gegrond op die interaksie van 'n laser pulse met 'n tyd-vertraagde kopie van homself. Die interaksie vind gewoonlik plaas binne in 'n $\chi^{(2)}$ medium.

Eksperimentele opstellings vir ALO en FOOH is ontwikkel wat gebruik maak van tweede harmoniek opwekking (THO). 'n Reeds bestaande IOK sisteem word gebruik vir puls karakterisasering in tyd. SGIOK resultate word verkry deur IOK data met behulp van 'n spesifieke Fourier filter te verwerk.

IOK en SGIOK metings van 'n kommersiële femtosekonde laser, dui aan dat die puls wat deur die laser uitgestraal word, 'n pulse lengte kleiner as 150 fs het en dat die pulse oor lineêre fase modulasie beskik. Hierdie resultate word deur die ALO en FOOH metings ondersteun.

'n 20 Hz fase gemoduleerde laser puls versterker (FMV) word ook gekarakteriseer. ALO metings van die FMV sisteem dui aan dat die puls wat deur hierdie sisteem uitgestraal word, egter 'n dubbel puls is. FOOH metings aan die ander kant, dui aan dat die puls se fase hoogs gemoduleer is.

Die eksperimente en fisiese interpretasies wat deur hierdie werk voorgestel word, toon die voorkeur metodes van optiese puls karaktarisering vir ultrakort laser pulse.

Acknowledgements

My sincere thanks goes to the following people and institutions for their contributions to this work:

- Prof. E. G. Rohwer and Prof. H. M. von Bergmann for their excellent supervision and endless fruitful discussions.

- The entire family of the LRI, for their support and friendship.

- All my fellow students, especially Gysbert Johannes van der Westhuizen, Dirk Spangenberg, Gareth David Dickenson, Anton Christiaan Nortje and Marguerite Blignaut for all the uhm, work related discussions.

- Pieter Herman Neethling for his steadfast advice on everything which was and is greatly appreciated.

- My house mate Alexander Matthias Heidt (the German), for conceptual help on this work.

- The Andrew Mellon Foundation for financial support.

- Prof. D. Jaroszynski from the University of Strathclyde for the use of the regenerative amplifier.

- My family and friends back in Knysna.

Contents

List of Figures

List of Tables

Chapter 1

Introduction

The discovery of stimulated optical emission from a ruby ($Cr:Al_2O_3$) crystal by Theodore Maiman in 1960 has been marked as the invention of the laser [1]. This discovery served as a pivotal point in the study of light-matter interaction, the reason being, that the laser now opened the world of coherent, high intensity light beams to researchers. These new light sources proved its value as early as 1961, when Franken et al showed that matter could react non-linearly to light radiation [2]. Motivated by this, researchers then spent the next twenty odd years in developing the laser as a reliable tool for scientific and industrial applications.

During the time period of 1964 to 1980, one of the most interesting developments in laser research was the generation of optical pulses with durations less then the cavity round-trip time of laser resonators [3]. During this time the first mode-locked lasers were developed using laser gain media such as Nd:Glass and Nd:YAG. These new types of solid-state lasers were capable of producing pulses with durations less than 100 ps [4, 5].

However, the first laser to develop sub-picosecond pulses was made from a continuous wave (cw) dye laser and not a solid state laser. Fork et al. showed that ultrashort pulses could be generated when a saturable absorber is introduced into a dye laser ring cavity [6]. This technique of ultrashort pulse generation was called colliding pulse mode-locking (CPM). Other laser

developments during the 1980's included the construction of a mode-locked laser with Ti:Sapphire as gain medium [7], and also chirped pulse amplification (CPA) techniques [8]. Ti:Sapphire mode-locked lasers soon became the research and industrial standard femtosecond laser. This was largely due to the fact that these mode-locked lasers could produce stable femtosecond pulses. The late 1990's and early 2000's saw the Ti:Sapphire mode-locked laser reach its pinnacle when it was reported that the theoretical pulse width limit of 5 fs for this laser was reached [9, 10].

Pulse characterization techniques evolved parallel to the advancement in ultrashort pulsed lasers. These techniques were initially only required to make estimates of the pulse width, but as the need for complete characterization increased, even phase information became necessary. The dawn of femtosecond pulses brought an end to electronic pulse characterization techniques. This is mostly because electronic devices such as the photo-diode can only achieve rise times in the order of 10 picoseconds (ps). For this reason, optical pulse characterization techniques were developed which exploit the fast non-linear optical response of materials. All of these optical techniques utilize the correlation of the pulse with either itself (autocorrelation) or a different pulse (cross-correlation) within a non-linear optical (NLO) medium. The type of interaction within the NLO medium, together with the detection of this interaction, sets the premise for the different optical pulse characterization techniques. These techniques include but are not limited to the following: interference autocorrelation (IAC) [11], spectral phase interferometry and direct electric field reconstruction (SPIDER) [12], frequency resolved optical gating (FROG) [13] and modified spectrum autointerferometric correlation (MOSAIC) [14].

The objective of this work was to develop techniques and apparatus to characterize ultrashort pulses emitted by a fs oscillator and a CPA. Pulse characterization will be shown through four methods all having their own distinct advantages. The methods are IAC, MOSAIC, background-free autocorrelation (BFA) and FROG. For the last two methods experimental setups were especially designed and constructed during the course of this work.

Chapter 2

Theory of Ultrashort Laser Pulses

Ultrashort laser pulses ($< 10^{-12}$ s) has made the study of non-linear optical effects resulting from light-matter interaction a standard in material characterization [15, 16, 17]. This is mainly due to the fact that these short laser pulses make peak intensities in excess of 100 GW/cm^2 easily accessible. The mechanisms of ultrashort pulse generation, description and characterization of short laser pulses will be addressed in the following sections.

2.1   Ultrashort Laser Pulse Generation

The generation of ultrashort laser pulses using solid state continuous wave (cw) lasers has been realized through various techniques [18, 19]. The most common techniques for generating optical pulses in the femtosecond (fs) regime are active and passive mode-locking, both being based on the principle of "locking" the longitudinal cavity modes in one or other way. The term mode-locking comes from the description of the laser output in the frequency domain, where the emitted radiation is considered to be made up of the sum of all the longitudinal cavity modes all having a certain fixed phase relation. This phase relation is achieved through either modulating the amplitudes or the frequencies of the cavity modes. Mode-locking of solid state lasers can be achieved through active or passive mode-locking techniques. Active mode-

3
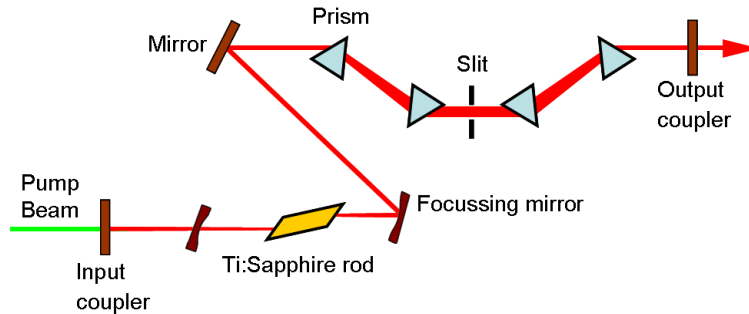
Figure 2.1: A schematic of a femtosecond laser cavity.

locking is a mode-locking technique in which an intra-cavity loss modulator is artificially introduced, whereas with passive mode-locking, the pulse itself generates a periodic modulation. Most modern day solid state fs mode-locked lasers use titanium doped sapphire (Ti:Al$_2$O$_3$) as laser gain medium. This is because Ti:Sapphire has an extremely broad emission band (from 660 to 1180 nm) due to lattice vibrations [7]. According to the Fourier theorem, the pulse duration is inversely proportional to the spectral width[1]. Therefore, the shortest theoretically achievable pulse duration for this medium amounts to 4fs.

The available longitudinal modes within these Ti:Sapphire laser cavities can be partially or totally locked in the active medium. This is a passive form of mode-locking and one example of this technique is based on the non-linear Kerr effect, sometime referred to as Kerr lens mode-locking (KLM) [20]. This effect is due to the third order nonlinear susceptibility tensor $\chi^{(3)}$ of the Ti:Sapphire crystal which induces an intensity dependent refractive index, $n = n_0 + n_2 I(\vec{r}, t)$, where n_2 is of the order of 10^{-16} cm^2/W. As a result, an intense cavity mode with a specific transverse intensity distribution will experience a transverse refractive index distribution when propagating through the active laser medium, which then acts as a focusing lens. Thus, cavity modes which randomly interfere constructively to form high intensity optical pulses will be focused stronger than the lower intensity cw cavity

---

[1]This relation will be derived in section (2.2.2).

modes. Consequently, femtosecond oscillators which exploit this phenomenon for mode-locking are designed such that losses are larger without the presence of this 'lens'. This is done through simply inserting a slit at the focal position of this induced lens (seen in fig.(2.1)).

In addition the presence of these intense laser pulses within the Ti:Sapphire crystal causes the refractive index to vary with time, thus leading to self-phase modulation (SPM). Thus, for a pulse propagating through a Ti:Sapphire crystal where $n_2 > 0$, it is found that the leading edge of the pulse is red shifted, whilst the trailing edge of the pulse is blue shifted [20]. The end result of this is a temporally and spectrally broadened pulse which can be compressed through introducing intra-cavity negative group velocity dispersion (GVD), by inserting a prism pair (as indicated in fig.(2.1)) or by chirped output couplers.

2.2 Theoretical Description of Laser Pulses

All forms of electromagnetic radiation are completely described by the time and space dependent electric field $\mathcal{E}(x, y, z, t)$. Therefore, a laser pulse being defined as a short burst of electromagnetic energy will also have an accompanying electric field distribution. Measurable quantities such as the intensity distribution and spectral intensity distribution of a laser pulse can directly be linked to the electric field, as will be seen in the following chapters. For theoretical description of electromagnetic pulse propagation, it becomes more convenient to write the electric field vector in a complex form, as it simplifies elaborate expressions. In the following two subsections the necessary definitions and notations which are used throughout this thesis will be summarized.

2.2.1 The Complex Representation

The electric field can be described in either time or frequency domain, and even though the measured quantities are real, it is normally more convenient

to use a complex representation of the electric field. Firstly, let us only consider the temporal dependence of the electric field, that is $\mathcal{E}(x, y, z, t) = \mathcal{E}(t)$. The real electric field $\mathcal{E}(t)$ can always be written as follows:

$$\mathcal{E}(t) = \overline{\mathcal{E}}(t) + c.c, \tag{2.1}$$

where $\overline{\mathcal{E}}(t)$ is defined as the complex electric field and $c.c$ its complex conjugate. This complex electric field $\overline{\mathcal{E}}(t)$ and the complex spectral field strength $\tilde{\mathcal{E}}(\omega)$, are linked to each other through the complex Fourier transform, $\mathcal{F}$:

$$\tilde{\mathcal{E}}(\omega) = \mathcal{F}\{\overline{\mathcal{E}}(t)\} = \int_{-\infty}^{\infty} \overline{\mathcal{E}}(t)e^{-i\omega t}dt = \left|\tilde{\mathcal{E}}(\omega)\right| e^{i\varphi(\omega)}, \tag{2.2}$$

where $\left|\tilde{\mathcal{E}}(\omega)\right|$ denotes the spectral amplitude, $\varphi(\omega)$ the spectral phase and ω the angular frequency. Henceforth, the time dependent complex electric field is obtained through taking the inverse Fourier transform $\mathcal{F}^{-1}$ of eq.(2.2):

$$\overline{\mathcal{E}}(t) = \mathcal{F}^{-1}\{\tilde{\mathcal{E}}(\omega)\} = \frac{1}{2\pi} \int_{-\infty}^{\infty} \tilde{\mathcal{E}}(\omega)e^{i\omega t}d\omega, \tag{2.3}$$

and also the time dependent real electric field through eq.(2.1). Eq.(2.3) however, requires $\tilde{\mathcal{E}}(\omega)$ to be non-zero for negative frequencies ω, which are practically not observed. This is remedied by redefining eq.(2.3) as:

$$\overline{\mathcal{E}}(t) = \frac{1}{2\pi} \int_{0}^{\infty} \tilde{\mathcal{E}}(\omega)e^{i\omega t}d\omega, \tag{2.4}$$

with a corresponding complex spectral field strength (or just complex spectral field) containing only positive frequencies:

$$\tilde{\mathcal{E}}(\omega) = \begin{cases} \left|\tilde{\mathcal{E}}(\omega)\right| e^{i\varphi(\omega)} & \text{for} \quad \omega \geq 0 \\ 0 & \text{for} \quad \omega < 0 \end{cases}. \tag{2.5}$$

In principle the bottom limit of the integral in eq.(2.4) can now again be replaced by $-\infty$. The spectral amplitude $\left|\tilde{\mathcal{E}}(\omega)\right|$ is practically always cen-

tered around some mean frequency ω_0 and will only have considerable values within a given frequency interval $\Delta\omega$ (also referred to as the bandwidth) which is small compared to ω_0. This implies that the complex electric field can now be written as:

$$\overline{\mathcal{E}}(t) = \frac{1}{2}E(t)e^{i\phi(t)}e^{i\omega_0 t} = \frac{1}{2}\bar{E}(t)e^{i\omega_0 t} \tag{2.6}$$

where $\phi(t)$ is the time dependent phase, ω_0 is now a carrier frequency, $E(t)$ is the field envelope and $\bar{E}(t)$ is the complex field envelope. Describing the field as is in eq.(2.6) and the convenience of an envelope description, is limited to the case where the bandwidth is minute compared to the carrier frequency:

$$\frac{\Delta\omega}{\omega_0} \ll 1. \tag{2.7}$$

Inequality (2.7) is satisfied when the temporal variation of $E(t)$ and $\phi(t)$ within an optical cycle $T = 2\pi/\omega_0$ is small. Consequently, the complex field envelope is then required to vary slowly with change in time, i.e.:

$$\left|\frac{d}{dt}\bar{E}(t)\right| \ll \omega_0\bar{E}(t) \tag{2.8}$$

The validity of the above inequality should be tested seeing that nowadays pulses containing only a few optical cycles are readily generated and studied [21].

In order to describe the physical meaning of the temporal phase $\phi(t)$, it is necessary to define a total instantaneous temporal phase:

$$\phi_{Total}(t) = \omega_0 t + \phi(t). \tag{2.9}$$

Accordingly, the derivative of this total phase establishes the time dependence of the carrier frequency (instantaneous frequency):

$$\omega_{inst}(t) = \frac{d}{dt}\phi_{Total}(t) = \omega_0 + \frac{d}{dt}\phi(t). \tag{2.10}$$
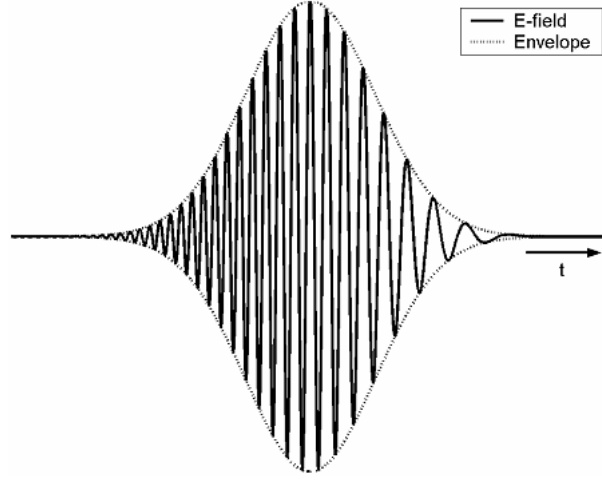
Figure 2.2: Electric field envelope (dotted line) and real part of the electric field (solid line) for a down-chirped pulse.

Hence if $d\phi/dt = b$, where b is a non-zero constant, this simply implies a correction of the carrier frequency by an amount of b in the form $\omega = \omega_0 + b$. If $d\phi/dt = f(t)$, this means that the carrier frequency changes with time and the corresponding field (or pulse) is frequency modulated or commonly referred to as being chirped. When $d^2\phi/dt^2 > (<)0$, the carrier frequency increases (decreases) with time, therefore the pulse is said to be up-chirped (down-chirped). In order to visualize the effect of chirp, fig.(2.2) shows a down-chirped pulse with an arbitrary envelope profile and carrier frequency. The choice of the ω_0 is not unique, but commonly it is identified as the carrier frequency at the pulse peak. There also exists a definition of ω_0, which is consistent in both the time and frequency domains, and is termed the intensity-weighted average frequency:

$$\omega_0 = \frac{\int_{-\infty}^{\infty} \omega_{inst}(t) \left| \bar{E}(t) \right|^2 dt}{\int_{-\infty}^{\infty} \left| \bar{E}(t) \right|^2 dt} = \frac{\int_{-\infty}^{\infty} \omega \left| \tilde{\mathcal{E}}(\omega) \right|^2 d\omega}{\int_{-\infty}^{\infty} \left| \tilde{\mathcal{E}}(\omega) \right|^2 d\omega}. \tag{2.11}$$

This statistical average frequency, is weighed against $\left| \bar{E}(t) \right|^2$ in the time domain and against $\left| \tilde{\mathcal{E}}(\omega) \right|^2$ in the frequency domain. These quantities are

referred to as the temporal and spectral intensities. A more complete description of the temporal intensity $(\mathrm{W/cm}^2)$ for a pulse traveling through a dispersionless material is:

$$
\begin{aligned}
I(t) &= \epsilon_0 cn \frac{1}{T} \int_{t-T/2}^{t+T/2} \mathcal{E}^2(t')dt' \\
&= \tfrac{1}{2}\epsilon_0 cn E^2(t) \\
&= \tfrac{1}{2}\epsilon_0 cn \left|\bar{E}(t)\right|^2
\end{aligned}
\tag{2.12}
$$

where ϵ_0 is the dielectric permittivity, n is the refractive index, c the speed of light in a vacuum and T is one optical period. The spectral intensity is obtained through applying Parseval's theorem[2] as:

$$
S_\omega(\omega) = \frac{\epsilon_0 cn}{\pi} \left|\tilde{\mathcal{E}}(\omega)\right|^2 .
\tag{2.13}
$$

In practice however, the spectral intensity is normally obtained through measurement as a function of wavelength, λ. In order to do this transformation from frequency to wavelength it is important to note that the spectral energy is the same whether it is calculated in frequency or wavelength:

$$
\int_{-\infty}^{\infty} S_\lambda(\lambda)d\lambda = \int_{-\infty}^{\infty} S_\omega(\omega)d\omega.
\tag{2.14}
$$

Knowing that $\omega = 2\pi c/\lambda$ and noting that $d\omega = -2\pi c/\lambda^2 d\lambda$, the right side of eq.(2.14) can be written as:

$$
\begin{aligned}
\int_{-\infty}^{\infty} S_\lambda(\lambda)d\lambda &= \int_{\infty}^{-\infty} S_\omega(2\pi c/\lambda)\frac{-2\pi c}{\lambda^2}d\lambda \\
&= \int_{-\infty}^{\infty} S_\omega(2\pi c/\lambda)\frac{2\pi c}{\lambda^2}d\lambda.
\end{aligned}
\tag{2.15}
$$

Eq.(2.15) implies that:

$$
S_\lambda(\lambda) = S_\omega(2\pi c/\lambda)\frac{2\pi c}{\lambda^2}.
\tag{2.16}
$$

---

[2]This theorem says that the energy should stay the same, when integrating over time or frequency.

The spectral phase in the frequency domain φ_ω relates to the spectral phase in the wavelength domain φ_λ as follows,

$$\varphi_\lambda(\lambda) = \varphi_\omega(2\pi c/\lambda) \tag{2.17}$$

which results merely in rescaling the spectral phase when transforming from one domain to the other. Note that the shape of the spectral intensity and the
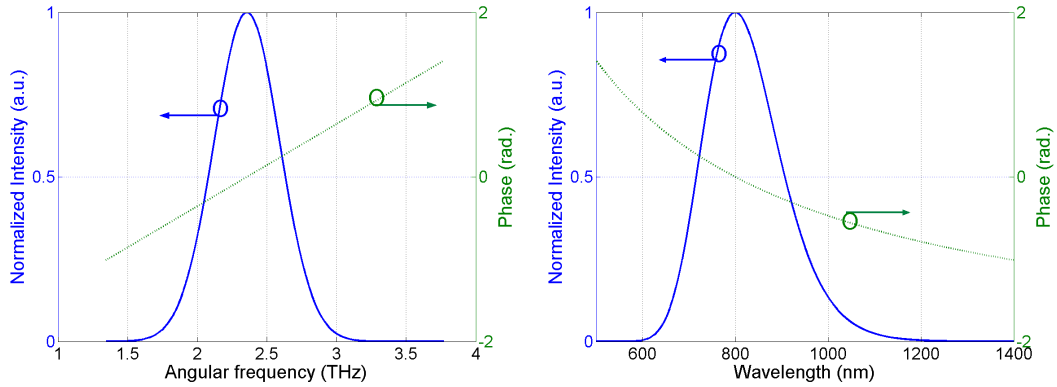
Figure 2.3: Two identical spectra and arbitrary spectral phases of a 5 fs pulse, plotted against angular frequency (left) and wavelength (right).

spectral phase in fig.(2.3) changes under transformation from frequency to wavelength and vice versa. It is also convenient sometimes to use quantities like the instantaneous pulse power $\mathcal{P}(t)$ (in Watt) derived from the Poynting theorem or the energy $\mathcal{W}$ (in Joule) [22]. The pulse power is merely the integral of the time-averaged intensity ($I(t)$) over its cross section ($\int_A dS$):

$$\mathcal{P}(t) = \int_A I(t)dS, \tag{2.18}$$

and a temporal integration of the power results in the energy,

$$\mathcal{W} = \int_{-\infty}^{\infty} \mathcal{P}(t)dt. \tag{2.19}$$

2.2.2 Pulse length and Spectral width

A quantitative measure of the length (or spread) of the temporal and spectral intensities is addressed in this section. The pulse length $\Delta\tau_p$ is a quantity which describes the duration of the laser pulse, whereas the spectral width $\Delta\omega_p$ gives its spectral content. There exist a number of different ways of defining the temporal and spectral widths of a pulse. One is to define $\Delta\tau_p$ and $\Delta\omega_p$ as "root-mean-squared (rms)" widths:

$$
\begin{aligned}
\Delta\tau_p(rms) &= \left[\frac{\int_{-\infty}^{\infty} t^2 I(t) dt}{\int_{-\infty}^{\infty} I(t) dt}\right]^{\frac{1}{2}} \\
\\
\Delta\omega_p(rms) &= \left[\frac{\int_{-\infty}^{\infty} \omega^2 S_\omega(\omega) d\omega}{\int_{-\infty}^{\infty} S_\omega(\omega) d\omega}\right]^{\frac{1}{2}}.
\end{aligned}
\tag{2.20}
$$

The advantage of the definitions in eq.(2.20) is that these integrals can normally be analytically solved. Experimentally however, extracting a rms-width is extremely difficult especially if the pulse has a complex structure. Another definition of $\Delta\tau_p$ and $\Delta\omega_p$ which is most generally used is the so-called "Full-Width-Half-Maximum (FWHM)". Within this definition, the temporal $\Delta\tau_p(FWHM)$ and spectral $\Delta\omega_p(FWHM)$ widths are merely the distances between the half-maximum points of $I(t)$ and $S(\omega)$, respectively. The field envelope $E(t)$, which through eq.(2.12) defines the shape of the temporal intensity $I(t)$, can be defined in various ways. The more commonly used pulse shapes are shown in table 2.1.

Profile:	$E(t)$	$\Delta\tau_p(FWHM)$
Gaussian Pulse	$\exp(-at^2)$	$\sqrt{2\ln 2/a}$
Sech Pulse	$\mathrm{sech}(at)$	$2\ln\left(\sqrt{2}+1\right)/a$
Lorentzian Pulse	$1/\left[1+(at)^2\right]$	$2\sqrt{\sqrt{2}-1}/a$
Two-sided exponential	$\exp(-\lvert at\rvert)$	$\ln 2/a$

Table 2.1: Field envelope profiles and FWHM relations.

As an example of how to determine the relation between a and $\Delta\tau_p(FWHM)$ consider the Gaussian field envelope in table 2.1. The temporal intensity $I(t)$

is then (from eq.(2.12)):

$$I(t) = \frac{1}{2}\epsilon_0 cn E^2(t) = \frac{1}{2}\epsilon_0 cn \exp(-2at^2). \qquad (2.21)$$

In order to calculate $\Delta\tau_p$ for the profile in eq. (2.21), it is firstly required to set the left side equal to $\frac{1}{2}I(0)$ and solve for t:

$$t = \sqrt{\frac{\ln 2}{2a}}. \qquad (2.22)$$

Thus according to the definition of the FWHM (as mentioned above), this width is simply equal to $2t$:

$$\Delta\tau_p(FWHM) = 2t = \sqrt{\frac{2\ln 2}{a}}. \qquad (2.23)$$

For this given Gaussian field envelope (in table 2.1) can be calculated the spectral width $\Delta\omega_p(FWHM)$. To facilitate this calculation, it is assumed that the time dependent phase varies quadratically with time i.e.:

$$\phi(t) = -bt^2 \qquad (2.24)$$

where b is a constant. The complex spectral field $\tilde{\mathcal{E}}(\omega)$ is then obtained through substituting the Gaussian field amplitude from table 2.1 together with eq.(2.24) into eq.(2.2) as:

$$\tilde{\mathcal{E}}(\omega) = \frac{\sqrt{\pi}}{a - ib} \exp\left[-\frac{(\omega - \omega_0)^2}{4(a - ib)}\right]. \qquad (2.25)$$

The spectral intensity (from eq.(2.13)) and spectral phase (from eq.(2.5)) can then be written as:

$$S_\omega(\omega) = \frac{\epsilon_0 cn}{a^2 + b^2} \exp\left[-\frac{a(\omega - \omega_0)^2}{2(a^2 + b^2)}\right], \qquad (2.26)$$

which has a Gaussian profile, and

$$\varphi(\omega) = \frac{b(\omega - \omega_0)^2}{2(a^2 + b^2)} \qquad (2.27)$$

where this spectral phase is also quadratic. Similarly to the calculation of $\Delta\tau_p(FWHM)$, the FWHM of $S_\omega(\omega)$ is:

$$\Delta\omega_p(FWHM) = 2\sqrt{2a\ln 2\left[1 + (b/a)^2\right]} \qquad (2.28)$$

In order to side-step bulky expressions, $\Delta\tau$ and $\Delta\omega$ will from this point be regarded as the FWHM of $I(t)$ and $S(\omega)$, respectively. Up to this stage, all the frequency dependent formulas have been written in terms of the angular frequency ω. Thus making use of the fact that $\omega = 2\pi f$, where f is the frequency in Hz, eq.(2.28) can subsequently be rewritten as:

$$\Delta f = \frac{\Delta\omega}{2\pi} = \frac{\sqrt{2\ln 2}}{\pi}\sqrt{a\left[1 + (b/a)^2\right]}. \qquad (2.29)$$

Field envelope	Temporal intensity	$\Delta\tau$ *(FWHM)*	Spectral intensity	$\Delta\tau$ *(FWHM)*	TBP
Gaussian	$\exp(-2at^2)$	$1.177/\sqrt{a}$	$\exp(-\frac{\omega^2}{2a})$	$2.355\sqrt{a}$	0.441
Sech	$\operatorname{sech}^2(at)$	$1.763/a$	$\operatorname{sech}^2(\frac{\pi\omega}{2a})$	$1.122a$	0.315
Lorentzian	$\left[1 + (at)^2\right]^{-2}$	$1.287/a$	$\exp(-\frac{2|\omega|}{a})$	$0.693a$	0.142
Two-sided exponential	$\exp(-2\,|at|)$	$0.693/a$	$\left[1 + (\frac{\omega}{a})^2\right]^{-2}$	$1.287a$	0.142

Table 2.2: Standard pulse profiles.

Seeing that the units of the pulse length is seconds (s) and that of the spectral width is per second (1/s or Hz), the product of these two values results in a dimensionless quantity. This quantity is known as the "Time-Bandwidth

Product (TBP)" and is dependent on the specific shapes of $I(t)$ and $S(\omega)$. The TBP for the Gaussian pulse profile under consideration is then (from eqs.(2.23) and (2.29)):

$$TBP = \Delta\tau\Delta f = \frac{2\ln 2}{\pi}\sqrt{\left[1 + (b/a)^2\right]}. \tag{2.30}$$

For an unchirped Gaussian pulse ($b = 0$) the TBP is thus approximately equal to 0.441, this pulse is consequently said to be "bandwidth-limited". The TBP for an unchirped Gaussian pulse, thus forms the limit of any TBP calculation for a Gaussian pulse with an arbitrary temporal (or spectral) phase. Table 2.2, which is taken taken from Diels et al [20], summarizes the normalized temporal intensities, normalized spectral intensities as well as the TBP's for given pulse envelopes in table 2.1.

2.3 Propagation

2.3.1 The Wave Equation

The propagation of laser pulses as well as the interaction with matter are governed by Maxwell's equations. When considering electromagnetic radiation in the absence of any current or static charge sources of the fields, Maxwell's equations in an infinite medium are [23]:

$$\nabla \times \boldsymbol{\mathcal{E}} = -\frac{\partial \boldsymbol{B}}{\partial t} \tag{2.31}$$

$$\nabla \times \boldsymbol{H} = \frac{\partial \boldsymbol{D}}{\partial t} \tag{2.32}$$

$$\nabla \cdot \boldsymbol{D} = 0 \tag{2.33}$$

$$\nabla \cdot \boldsymbol{B} = 0 \tag{2.34}$$

with

$$\boldsymbol{D} = \varepsilon_0\boldsymbol{\mathcal{E}} + \boldsymbol{P} \tag{2.35}$$

$$\boldsymbol{B} = \mu_0(\boldsymbol{H} + \boldsymbol{M}) \tag{2.36}$$

where $\boldsymbol{\mathcal{E}}$ is the electric field, $\boldsymbol{H}$ the magnetic field, $\boldsymbol{D}$ the electric displacement, $\boldsymbol{B}$ the magnetic induction, $\boldsymbol{P}$ the polarization vector, $\boldsymbol{M}$ the magnetization vector, ε_0 the dielectric constant of vacuum and μ_0 the permeability constant of vacuum. Time and spacial dependence is assumed for all the vector quantities.

The polarization vector $\boldsymbol{P}$ describes the response of matter to electromagnetic radiation and is generally written in its component form as a power series of the electric field $\boldsymbol{E}$ as [24]:

$$
\begin{aligned}
P_i &= \varepsilon_0 \chi_{ij}^{(1)} \mathcal{E}_j + 2\chi_{ijk}^{(2)} \mathcal{E}_j \mathcal{E}_k + 4\chi_{ijkl}^{(3)} \mathcal{E}_j \mathcal{E}_k \mathcal{E}_l + \cdots \\
&= P_i^L + P_i^{NL}
\end{aligned}
\tag{2.37}
$$

where the first term on the right is called the linear polarization (P_i^L-ith component), the second term the second-order nonlinear polarization and the third term the third-order nonlinear polarization (summarized as P_i^{NL}-ith component). Summations are assumed over repeated indices. $\chi^{(1)}$ is the linear susceptibility, $\chi^{(2)}$ and $\chi^{(3)}$ are the second- and third-order susceptibility, respectively. These susceptibility terms are tensor quantities and relate how a particular medium reacts to radiation of electromagnetic waves. The exact form of these susceptibility tensors can be determined through group theoretical studies [25].

Assuming a nonmagnetic medium ($\boldsymbol{M} = \boldsymbol{0}$) the magnetic induction becomes (from eq.(2.36)):

$$\boldsymbol{B} = \mu_0 \boldsymbol{H} \tag{2.38}$$

Introducing eqs.(2.38) and (2.35) into eqs. (2.31) and (2.32) and applying the relevant mathematical identity[3], the wave equation for an electric field

---

[3]Vector second derivative: $\nabla \times \nabla \times \tilde{\mathcal{E}} = \nabla(\nabla \cdot \tilde{\mathcal{E}}) - \nabla^2 \tilde{\mathcal{E}}$.

in a nonmagnetic material is obtained as:

$$\left[\nabla^2 - \frac{1}{c^2}\frac{\partial^2}{\partial t^2}\right]\boldsymbol{E}(x,y,z,t) = \mu_0\frac{\partial^2\boldsymbol{P}(x,y,z,t)}{\partial t^2} \tag{2.39}$$

where $c = 1/\sqrt{\varepsilon_0\mu_0}$ is the speed of light in a vacuum. In eq.(2.39) it is clear that the polarization of the medium acts as a source for new electric field. This forms the basis of light-matter interaction, whereby upon radiation of a material with light, the medium is polarized and essentially generates new electromagnetic radiation.

2.3.2 Linear Propagation

The complexity of eq.(2.39) makes solving it analytically, impossible. Thus it is generally solved by numerical methods. However, through appropriate approximations a much simpler reduced form can be derived, to deal with many pulse propagation problems. For this purpose, it is assumed that the electric field is linearly polarized and propagates in the z-direction as a plane wave, that is to say that the field is uniform in the in the x and y-directions. The wave equation, eq.(2.39), is now simplified to:

$$\left[\frac{\partial^2}{\partial z^2} - \frac{1}{c^2}\frac{\partial^2}{\partial t^2}\right]\mathcal{E}(z,t) = \mu_0\frac{\partial^2 P^L(z,t)}{\partial t^2}. \tag{2.40}$$

Here it is explicitly assumed that the medium under investigation responds linearly to electromagnetic radiation. The expression for the linear polarization in the frequency domain (similar to the definition in eq.(2.37)) is:

$$\tilde{P}^L(\omega,z) = \varepsilon_0\chi^{(1)}(\omega)\tilde{\mathcal{E}}(\omega,z). \tag{2.41}$$

The assumption of a plane wave (as mentioned above) implies harmonic time dependence of the form, $e^{-i\omega t}$, for arbitrary solutions to eq.(2.40). Keeping this time dependence in mind, and taking the Fourier transform of eq.(2.40)

together with eq.(2.41) results in:

$$\left[\frac{\partial^2}{\partial z^2} - \frac{\omega^2}{c^2}\varepsilon(\omega) \right] \tilde{\mathcal{E}}(\omega, z) = 0 \tag{2.42}$$

where the dielectric constant is

$$\varepsilon(\omega) = 1 + \chi^{(1)}(\omega). \tag{2.43}$$

Here it is assumed that both the dielectric constant and linear susceptibility are real. A general solution of eq.(2.42) for propagation through a dispersive medium with refractive index $n(\omega)$ along the positive z-direction is:

$$\tilde{\mathcal{E}}(\omega, z) = \tilde{\mathcal{E}}(\omega, 0)e^{-i\beta(\omega)z} \tag{2.44}$$

where $\beta(\omega)$ is the propagation constant and is defined as,

$$\beta(\omega) = \frac{\omega}{c}\sqrt{\varepsilon(\omega)} = \frac{\omega}{c}n(\omega). \tag{2.45}$$

Normally, only narrow bandwidth fields are considered, with all its frequency components mainly close to some center frequency ω_0. The propagation constant can thus be expanded about its value at ω_0,

$$\beta(\omega) = \beta_0 + \beta' \times (\omega - \omega_0) + \frac{1}{2}\beta'' \times (\omega - \omega_0)^2 + \ldots = \beta_0 + \delta\beta \tag{2.46}$$

where $\beta' \equiv d\beta/d\omega$ and $\beta'' \equiv d^2\beta/d\omega^2$ are both centered at ω_0. The coefficients in the Taylor expansion of the propagation constant have the following

meanings:

$$
\begin{aligned}
\beta_0 &= \beta(\omega)\mid_{\omega=\omega_0} &= \frac{\omega_0}{v_p(\omega_0)} &\equiv \frac{\omega_0}{\text{phase velocity}} \\[2mm]
\beta' &= \frac{d\beta}{d\omega}\mid_{\omega=\omega_0} &= \frac{1}{v_g(\omega_0)} &\equiv \frac{1}{\text{group velocity}} \\[2mm]
\beta'' &= \frac{d^2\beta}{d\omega^2}\mid_{\omega=\omega_0} &= \frac{d}{d\omega}\left(\frac{1}{v_g(\omega_0)}\right) &\equiv \text{``group velocity dispersion (GVD)''.}
\end{aligned}
\tag{2.47}
$$

Inserting eq.(2.46) into eq.(2.44) yields,

$$
\tilde{\mathcal{E}}(\omega, z) = \tilde{\mathcal{E}}(\omega, 0)e^{-i\beta_0 z}e^{-i\delta\beta z}.
\tag{2.48}
$$

Analogous to the introduction of a slowly varying envelope function in time (eqs.(2.6) to (2.8)), a Fourier amplitude having only appreciable values in a small interval $\partial\beta$ centered at β_0, which varies slowly with the spatial coordinate can now be defined:

$$
\tilde{E}(\omega', z) = \tilde{\mathcal{E}}(\omega, 0)e^{-i\delta\beta z}
\tag{2.49}
$$

where $\omega' = \omega + \omega_0$. Still, this treatment is only useful for the case,

$$
\left|\frac{d}{dz}\tilde{E}(\omega', z)\right| \ll \beta_0\left|\tilde{E}(\omega', z)\right|
\tag{2.50}
$$

which implies that the wave number spectrum is sufficiently small

$$
\left|\frac{\partial\beta}{\beta_0}\right| \ll 1.
\tag{2.51}
$$

This means that the pulse envelope must not change considerably while traveling a distance equivalent to the wavelength $\lambda_0 = 2\pi/\beta_0$. The inverse Fourier transform of eq.(2.48) can be written as,

$$
\overline{\mathcal{E}}(t, z) = \frac{1}{2}\bar{E}(t, z)e^{i(\omega_0 t - \beta_0 z)}
\tag{2.52}
$$

where

$$\bar{E}(t,z) = \frac{1}{\pi} \int_{-\infty}^{\infty} \tilde{\mathcal{E}}(\omega,0) e^{i(\omega-\omega_0)t} e^{-i\delta\beta z} d\omega \tag{2.53}$$

is the envelope varying slowly in time and space. For further simplifications to the wave equation (eq.(2.40)) it is required that the linear polarization $P^L(z,t)$ is written in terms of the slowly varying amplitude $\bar{E}(t,z)$. This is achieved through expanding $\varepsilon(\omega)$ as a series around ω_0 and introducing it into eq.(2.41) which leads to,

$$\tilde{P}^L(\omega,z) = \varepsilon_0 \left(\varepsilon(\omega_0) - 1 + \sum_{n=1}^{\infty} \frac{1}{n!} \frac{d^n\varepsilon}{d\omega^n} \mid_{\omega_0} (\omega-\omega_0)^n \right) \tilde{\mathcal{E}}(\omega,z) \tag{2.54}$$

and then determining the corresponding expression in the time domain as,

$$\begin{aligned} P^L(t,z) &= \tfrac{1}{2} \left\{ \varepsilon_0 \left[\varepsilon(\omega_0) - 1 \right] \bar{E}(t,z) \right. \\ &+ \left. \varepsilon_0 \sum_{n=1}^{\infty} (-i)^n \tfrac{1}{n!} \tfrac{d^n\varepsilon}{d\omega^n} \mid_{\omega_0} \tfrac{\partial^n}{\partial t^n} \bar{E}(t,z) \right\} e^{i(\omega_0 t - \beta_0 z)}. \end{aligned} \tag{2.55}$$

In order to form a wave equation capable of dealing with a field envelope varying slowly in time and space, eqs.(2.52) and (2.55) are substituted into the wave equation eq.(2.40), together with a coordinate transformation into a reference framework (η, ξ) moving at the group velocity v_g. The coordinate transformation from (z,t) to (η, ξ) occurs as follows:

$$\xi = z \qquad \eta = t - \tfrac{z}{v_g} \tag{2.56}$$

with new space-time derivatives,

$$\tfrac{\partial}{\partial z} = \tfrac{\partial}{\partial \xi} - \tfrac{1}{v_g} \tfrac{\partial}{\partial \eta} \qquad \qquad \tfrac{\partial}{\partial t} = \tfrac{\partial}{\partial \eta} \ . \tag{2.57}$$

The wave equation then becomes,

$$\frac{\partial}{\partial \xi} \bar{E} - \frac{i}{2} \beta'' \frac{\partial^2}{\partial \eta^2} \bar{E} + \mathcal{D} = -\frac{i}{2\beta_0} \frac{\partial}{\partial \xi} \left(\frac{\partial}{\partial \xi} - \frac{2}{v_g} \frac{\partial}{\partial \eta} \right) \bar{E} \tag{2.58}$$

where

$$
\begin{aligned}
\mathcal{D} \;=\;& \frac{i}{3\beta_0 c^2} \sum_{n=3}^{\infty} \frac{(-i)^n}{n!} \left\{ \omega_0^2 \frac{d^n \varepsilon}{d\omega^n} \mid_{\omega_0} + 2n\omega_0 \frac{d^{(n-1)}\varepsilon}{d\omega^{(n-1)}} \mid_{\omega_0} \right. \\
& \left. + \; n(n-1)\, \frac{d^{(n-2)}\varepsilon}{d\omega^{(n-2)}} \mid_{\omega_0} \right\} \frac{\partial^2}{\partial \eta^2} \bar{E}.
\end{aligned}
\tag{2.59}
$$

The expression on the right of eq.(2.58) can be neglected when exploiting the envelope properties eqs.(2.8) and (2.50). The quantity $\mathcal{D}$ can also be neglected when assuming that the dielectric constant changes slowly over the frequencies within the pulse spectrum. These simplifications lead to a greatly simplified wave equation:

$$
\frac{\partial}{\partial \xi} \bar{E} - \frac{i}{2} \beta'' \frac{\partial^2}{\partial \eta^2} \bar{E} = 0
\tag{2.60}
$$

which describes how the complex pulse envelope evolves as it propagates through a lossless medium with group velocity dispersion (GVD). This procedure is commonly termed slowly varying envelope approximation (SVEA), which essentially reduces the wave equation to first-order derivatives with respect to the spatial coordinate.

For zero GVD ($\beta'' = 0$) the complex pulse envelope $\bar{E}(\eta, \xi)$ does not change as it propagates. For nonzero GVD ($\beta'' \neq 0$) eq.(2.60) can be solved in the frequency domain by taking the its Fourier transformation as:

$$
\tilde{E}(\omega, z) = \tilde{E}(\omega, 0) e^{-\frac{i}{2}\beta''\omega^2 z}.
\tag{2.61}
$$

The temporal complex pulse envelope is thus given as,

$$
\bar{E}(z, t) = \mathcal{F}^{-1} \left\{ \tilde{E}(\omega, 0) e^{-\frac{i}{2}\beta''\omega^2 z} \right\}.
\tag{2.62}
$$

To illustrate the effect GVD has on a pulse, consider the linearly chirped Gaussian pulse described in eqs.(2.24) and (2.25). The spatially dependent field spectrum is then obtained by simply inserting eq.(2.25) into eq.(2.61) yielding:

$$
\tilde{E}(\omega, z) = \tilde{E}_0 e^{-\alpha\omega^2} e^{-i\gamma\omega^2}
\tag{2.63}
$$

where

$$\alpha = \frac{a}{4(a^2 + b^2)} \tag{2.64}$$

and

$$\gamma(z) = \frac{b}{4(a^2 + b^2)} + \frac{\beta'' z}{2}. \tag{2.65}$$

and $\tilde{E}_0$ forms the complex amplitude factor. Inserting eq.(2.63) into eq.(2.62) and calculating the Fourier transforms leads to the following expression for the time and space dependent electric field:

$$\bar{E}(z,t) = \bar{E}_0 \exp\left\{-\left(1 + i\frac{\gamma(z)}{\alpha}\right)\left(\frac{t}{\sqrt{\frac{4}{\alpha}\left[\alpha^2 + \gamma^2(z)\right]}}\right)^2\right\}. \tag{2.66}$$

Eq.(2.66) can however be rewritten as,

$$\bar{E}(z,t) = \bar{E}_0 \exp\left\{-\left(\rho(z)t^2 + i\phi(t,z)\right)\right\} \tag{2.67}$$

with a pulse duration of

$$\Delta\tau(z) = \sqrt{\frac{2\ln 2}{\rho(z)}} = \sqrt{\frac{8\ln 2}{\alpha}\left[\alpha^2 + \gamma^2(z)\right]} \tag{2.68}$$

and temporal modulation (or chirp)

$$\phi(t,z) = -\frac{\gamma^2(z)}{4\left[\alpha^2 + \gamma^2(z)\right]}t^2 \tag{2.69}$$

which resembles again a linearly chirped Gaussian pulse. The effect of GVD on an initially positively chirped ($b > 0$) input pulse of duration $\Delta\tau$ after propagating a distance of z can now be deduced from eqs.(2.65) and (2.68) as:

$$\beta'' > 0 \quad \Rightarrow \quad \Delta\tau(z) > \Delta\tau \quad \Rightarrow \quad \text{pulse broadening}$$

$$\tag{2.70}$$

$$\beta'' < 0 \quad \Rightarrow \quad \Delta\tau(z) < \Delta\tau \quad \Rightarrow \quad \text{pulse compression.}$$
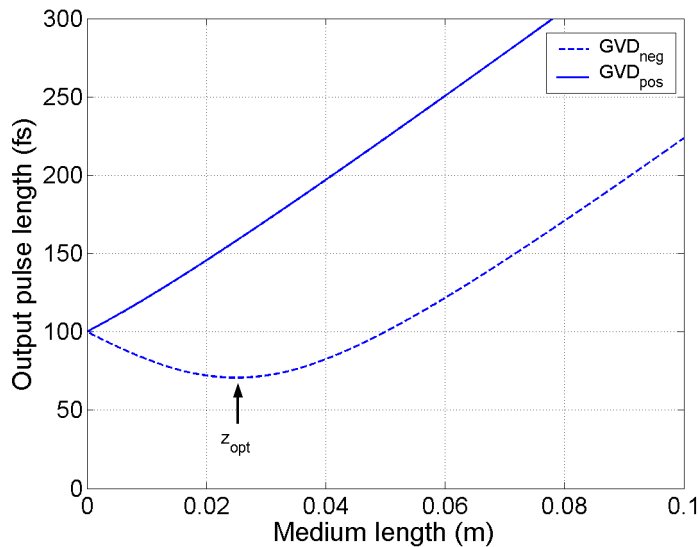
Figure 2.4: The effect of GVD on the pulse duration of a 100fs chirped pulse through a dispersive medium with $|\beta''| \approx 72\text{fs}^2/\text{mm}$.

Note however, that pulse compression has an optimum value which is limited by the initial chirp parameter b as well as an optimum propagation distance z_{opt}. After this distance, pulse broadening occurs, even with $\beta'' < 0$. The above argument is graphically illustrated in fig.(2.4) for both positive and negative GVD.

2.3.3 Nonlinear Propagation

In this section the nonlinear phenomenon of the generation of second harmonic light will be studied. Second harmonic generation (SHG) describes the effect in which light with an initial frequency ω is incident upon a nonlinear optical (NLO) material, which results in the generation (in transmission or reflection) of light with a frequency of 2ω. The first experimental demonstration of SHG was shown by Franken et al in 1961 [2]. They used a ruby laser with a center wavelength of $\lambda = 694$ nm, and focused its beam into a quartz crystal where the second harmonic (SH) light was generated. The generated SH light was then separated from the fundamental by the use of a

prism, which spatially separated the beams (ω and 2ω). The light was then subsequently detected on a photographic plate.
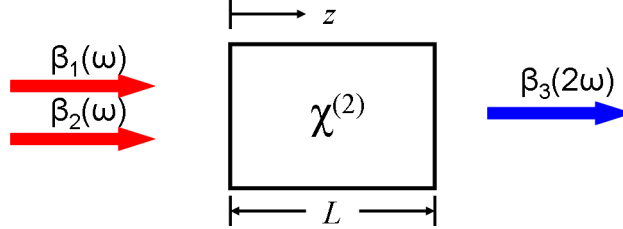
Figure 2.5: Schematic depiction of second harmonic generation in a $\chi^{(2)}$-medium with length L.

2.3.3.1   Second Harmonic Generation

The assumed configuration of the SHG is shown in fig.(2.5), where the applied linearly polarized (in the z-direction) monochromatic waves with propagation constants $\beta_1(\omega)$ and $\beta_2(\omega)$ incident on a lossless nonlinear medium at normal incidence. The presence of these plane waves in the medium results in a nonlinear source term in eq.(2.39) as:

$$P^{NL}(z,t) = P_3 e^{-i2\omega t} \tag{2.71}$$

where according to eq.(2.37)

$$P_3 = 2\chi^{(2)}_{eff}\bar{E}_1\bar{E}_2 \tag{2.72}$$

for an effective second-order susceptibility $\chi^{(2)}_{eff}$ due to propagation in the z-direction only. The applied fields used in eq.(2.71) were represented as:

$$\overline{\mathcal{E}}_j(t,z) = \bar{E}_j(z)e^{-i\omega t} \qquad j = 1,2 \tag{2.73}$$

where

$$\bar{E}_j(z) = A_j(z)e^{i\beta_j(\omega)z} \qquad j = 1,2. \tag{2.74}$$

The amplitude of the nonlinear polarization (eq.(2.72)) can thus be rewritten as:

$$P_3 = 2\chi_{eff}^{(2)} A_1(z) A_2(z) e^{i(\beta_1(\omega) + \beta_2(\omega))z}. \tag{2.75}$$

Substituting eqs.(2.71) and (2.72) into the wave equation eq.(2.39) and assuming only z-dependence of field in its spatial coordinates leads to:

$$\left[\frac{d^2}{dz^2} - \frac{1}{c^2} \frac{\partial^2}{\partial t^2} \right] \overline{\mathcal{E}}_3(t, z) = -2\chi_{eff}^{(2)} \mu_0 (2\omega)^2 A_1(z) A_2(z) e^{i[(\beta_1(\omega) + \beta_2(\omega))z - 2\omega t]}, \tag{2.76}$$

where $\overline{\mathcal{E}}_3(t, z)$, the generated SH electric field, has the following form,

$$\overline{\mathcal{E}}_3(t, z) = A_3(z) e^{i(\beta_3(2\omega)z + i2\omega t)} \tag{2.77}$$

with propagation constant,

$$\beta_3(2\omega) = \frac{2\omega n_3(2\omega)}{c} \tag{2.78}$$

and a yet to be determined amplitude $A_3(z)$.

The generated SH electric field expression in eq.(2.77) is a solution for eq.(2.39) in the absence of source terms where A_3 a constant. Therefore, in the presence of small nonlinear source terms the solution will also be of the form in eq.(2.77), however A_3 is now a slowly varying function of z. Eq.(2.76) within the SVEA for A_3 can thus be simplified to:

$$\frac{dA_3(z)}{dz} = \frac{2i\chi_{eff}^{(2)} \mu_0 \omega c}{n_3(2\omega)} A_1(z) A_2(z) e^{i\Delta\beta z} \tag{2.79}$$

where the wavevector (or momentum) mismatch is introduced as,

$$\Delta\beta = (\beta_2(\omega) + \beta_1(\omega)) - \beta_3(2\omega). \tag{2.80}$$

Eq.(2.79) is known as the coupled-amplitude equation, because it describes how the amplitude of the generated SH wave varies with the coupling of the

amplitudes of the applied electric fields.

2.3.3.2 Phase-matching

Phase-matching on a microscopic level occurs when individual atomic dipoles within a medium are well phased such that the emitted radiation from each dipole coherently add up in the forward direction. Perfect phase-matching is achieved when there is no wavevector mismatch i.e.:

$$\Delta\beta = 0. \tag{2.81}$$

Under this condition (eq.(2.81)), when assuming an undepleted pump model for SHG - which implies that the amplitudes A_1 and A_2 of the applied fields are assumed constant - the amplitude A_3 (from eq.(2.79)) of the SH wave increases linearly with z, and subsequently the intensity increases quadratically with z.

However, when the perfect phase-matching condition (eq.(2.81)) for an undepleted pump approximation is not satisfied, the intensity of the SH wave for a medium of length L is obtained by integrating eq.(2.79) from $z = 0$ to $z = L$ which yields:

$$I_3 = \frac{8\chi_{eff}^2\mu_0^3c^3\omega^2}{n_1(\omega)n_2(\omega)n_3(2\omega)}I_1I_2L^2\text{sinc}^2(\Delta\beta L/2) \tag{2.82}$$

where (from eq.(2.12)),

$$I_i = \tfrac{1}{2}\varepsilon n_i c \left|A_i\right|^2 \qquad i = 1, 2, 3. \tag{2.83}$$

The efficiency of the SH process is given solely by the $\text{sinc}^2(\Delta\beta L/2)$ factor in eq.(2.82) which depends on the wavevector mismatch as well as the medium length. As seen in fig.(2.6), the efficiency of SHG decreases sharply as $\Delta\beta$ increases. What is also evident from fig.(2.6) is that the medium length plays a crucial role in the sensitivity for obtaining SH light when nearly perfectly
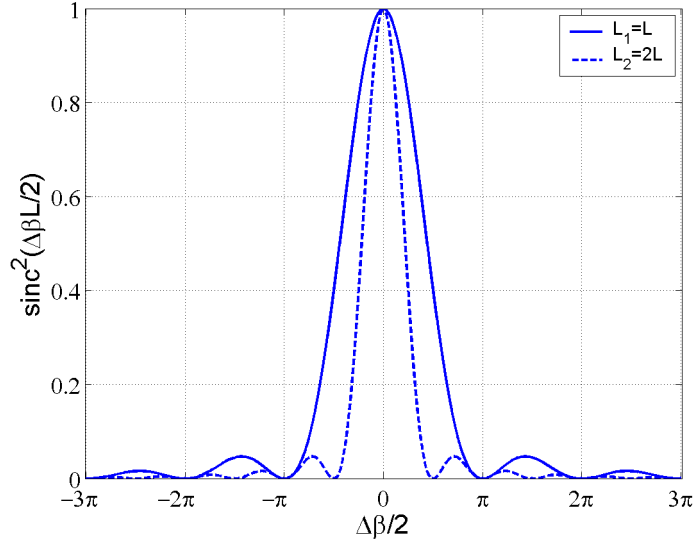
Figure 2.6: Effect of wavevector mismatch on the efficiency of SHG for a medium of length L (solid line) and a medium of length $2L$ (dashed line).

phase-matched. In other words, the efficiency of SHG in longer NLO mediums decreases significantly when $\Delta\beta \neq 0$, even though these longer mediums guarantee (from the L^2 behaviour of eq.(2.82)) more SH light intensity. Another important result of eq.(2.82) is that the intensity of the generated SH light varies quadratically with the input fundamental field intensity (in the case where $I_1 = I_2$). This result is often used in order to check whether SHG has occurred or not.

For SHG, there exists however, a better approximation for the intensity of SH light, which assumes that the input field amplitudes decrease as they travel through a NLO medium- this is the so-called depleted pump model. In this model it is assumed that $\Delta\beta = 0$. This perfectly phase-matched condition for SHG implies however that:

$$(\beta_2(\omega) + \beta_1(\omega)) - \beta_3(2\omega) = 0 \qquad (2.84)$$

which, when assuming that the two applied fields in fig.(2.5) have the same polarization, direction ($\beta_1 = \beta_2 = \beta$) and also inserting eq.(2.45), simplifies

to

$$n(\omega) = n_3(2\omega). \tag{2.85}$$

Note that eq.(2.85) describes the perfect phase-matching condition for collinear arranged input fields only, which is not always the arrangement of choice[4]. This condition in eq.(2.85) can however not be achieved, because in most loss-less materials the index of refraction is an increasing function of frequency. This effect is more commonly known as normal dispersion.

In order to bypass this problem, anomalous dispersion within some materials can be exploited. Anomalous dispersion is an effect which is extremely pronounced around an absorption feature of a medium, where the refractive index decreases with increasing frequencies. Another, more commonly used procedure to achieve perfect phase matching is to make use of the phenomenon of birefringence displayed in many crystals. Birefringence is understood to be the dependence of the refractive index on the polarization direction of the light waves which propagate through the medium. Crystals
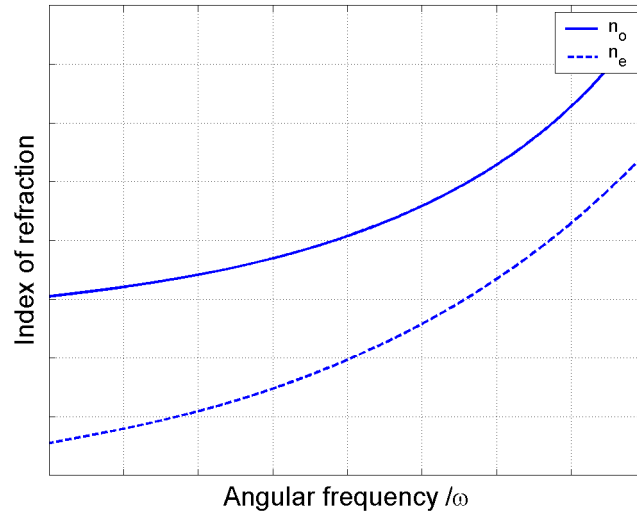

Figure 2.7: Illustration of dispersion of the refractive index for a negative uniaxial crystal.

---

[4]See section 4.3.

not belonging to the cubic crystal system, like uniaxial or biaxial crystals, all show the effect of birefringence. Consider the example of an uniaxial crystal where light waves can experience ordinary n_o or extraordinary n_e refractive indices. Phase-matching in these crystals for SHG can be achieved by allowing the SH light to be polarized such that it experiences the lowest refractive index. Fig.(2.7) shows how the refractive index (both n_o and n_e) for a negative ($n_o > n_e$) uniaxial crystal varies with frequency. Conversely, positive uniaxial crystals are simply defined as uniaxial crystals with $n_o < n_e$. Uniaxial crystals are characterized by a directional vector (say $\hat{c}$) the so-called optical axis (seen in fig.(2.8)). Light which is perpendicularly polarized to the plane containing the optical axis $\hat{c}$ and propagation direction $\hat{z}$ is said to be ordinary polarized, and subsequently experiences an ordinary index of refraction n_o. Light which is polarized parallel to the plane containing vectors $\hat{c}$ and $\hat{z}$ is said to be extraordinarily polarized. This extraordinary polarization leads to the light waves experiencing an extraordinary index of refraction n_e. There exist two ways in which phase-matching for the purposes
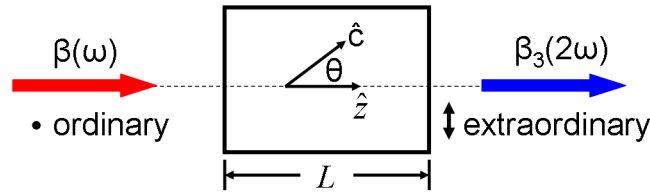
Figure 2.8: Schematic of SHG through angle-tuned phase matching.

of SHG in negative uniaxial crystals can be accomplished, remembering that SH light generated from negative uniaxial crystals should experience an extraordinary refractive index n_e. The first method requires that the two input fields (from fig.(2.5)) are polarized such that they experience ordinary refractive indices, this is commonly termed as type I phase-matching. The second method requires that one of the input fields is ordinarily polarized, whilst the other is extraordinarily polarized. This method is termed type II phase-matching. Table 2.3 summarizes the phase-matching possibilities for positive and negative uniaxial crystals. From table 2.3 it is evident that for

Phase-matching	Positive Uniaxial $n_o < n_e$	Negative Uniaxial $n_o > n_e$
Type I	$2n_3^o(2\omega) = n_1^e(\omega) + n_2^e(\omega)$	$2n_3^e(2\omega) = n_1^o(\omega) + n_2^o(\omega)$
Type II	$2n_3^o(2\omega) = n_1^o(\omega) + n_2^e(\omega)$	$2n_3^e(2\omega) = n_1^e(\omega) + n_2^o(\omega)$

Table 2.3: Phase-matching condition for SHG in uniaxial crystals.

effective phase-matching to be achieved, it is required to control the refractive indices at the fundamental frequency ω, as well as at the second harmonic frequency 2ω. For uniaxial crystals, the degree of birefringence can be altered by changing the crystals orientation with respect to the input fields, or through changing the temperature of the crystal. These two methods are commonly referred to as angle tuning and temperature tuning.

Considering angular tuning for uniaxial crystal only, from fig.(2.8) and the definition of extraordinary polarization, it is easy to conclude that light polarized as such experiences an extraordinary refractive index $n_e(\theta)$ which depends on the angle θ between the propagation direction $\hat{z}$ and the optical axis $\hat{c}$. This relation is given by Boyd [25] as:

$$\frac{1}{n_e^2(\theta)} = \frac{\sin^2\theta}{\bar{n}_e^2} + \frac{\cos^2\theta}{n_o^2} \tag{2.86}$$

where $\bar{n}_e$ is the principle value of the extraordinary refractive index. It is important to note that for $\theta = 90^o$ the extraordinary refractive index is equal to its principle value, and for $\theta = 0^o$ it is equal to the ordinary refractive index. Successful phase-matching for SHG is achieved by changing the angle θ such that the perfect phase-matching condition, $\Delta\beta = 0$ is fulfilled. For SHG in negative uniaxial crystals eq.(2.86) simplifies to,

$$\sin^2\theta = \frac{\frac{1}{n_o^2(\omega)} - \frac{1}{n_o^2(2\omega)}}{\frac{1}{\bar{n}_e^2(2\omega)} - \frac{1}{n_o^2(2\omega)}} \tag{2.87}$$

which shows how the crystal should be orientated. Eq.(2.87) however does not always have a real solution, for arbitrary conditions.

Chapter 3

Characterization Techniques of Ultrashort Laser Pulses

The incapability of opto-electronic devices to measure optical pulse durations shorter than a couple of picoseconds has prompted the development of optical pulse measurement techniques capable of measuring sub femtosecond pulse durations. The optical techniques which will be discussed in this chapter, are all examples of second-order autocorrelation techniques. The term "second-order" indicates that these techniques exploit the second-order nonlinear polarization $P_{2\omega}^{NL}(t)$ of NLO materials. The term "autocorrelation" implies that the pulse to be investigated is compared with a time-delayed copy of itself, as apposed to cross-correlation where the pulse is compared to a different reference pulse. Depending on how the pulse is compared to the time-delayed copy of itself, second-order autocorrelation can be split into two groups, namely interferometric autocorrelation (IAC) or intensity autocorrelation (IntenAC). Considering firstly second-order IAC ofLLLLlllllllllllllllllllllllllllllllllll a laser pulse with an electric field $\mathcal{E}(t)$, the expression which describes the autocorrelation is taken from Diels et al [20]:

$$G^{(2)}(\tau) = \int_{-\infty}^{\infty} \left| [\mathcal{E}(t) + \mathcal{E}(t - \tau)]^2 \right|^2 dt \tag{3.1}$$

where τ describes the time-delay between the pulse and its copy. The specific form of $G^{(2)}(\tau)$ can be understood when noting that,

$$P_{2\omega}^{NL}(t,\tau) = 2\chi^{(2)}\mathcal{E}(t-\tau)\mathcal{E}(t) \qquad (3.2)$$

(from eq.(2.37), (2.79) and (2.82)) which results in $G^{(2)} \propto \left(P_{2\omega}^{NL}\right)^2$. This means that the second-order IAC function records how the intensity of a second-order interaction between two pulses varies with τ. Eq.(3.1) can be decomposed further by introducing the amplitude and phase dependence of the laser pulse as described in eq.(2.6) to:

$$G^{(2)}(\tau) = C_0(\tau) + \Re\left\{4C_1(\tau)e^{i\omega_0\tau}\right\} + \Re\left\{2C_2(\tau)e^{i2\omega_0\tau}\right\} \qquad (3.3)$$

where

$$C_0(\tau) = \int_{-\infty}^{\infty} dt \left\{E^4(t-\tau) + E^4(t) + 4E^2(t-\tau)E^2(t)\right\}, \qquad (3.4)$$

$$C_1(\tau) = \int_{-\infty}^{\infty} dt \left\{E(t-\tau)E(t)\left[E^2(t-\tau) + E^2(t)\right]e^{i[\phi(t-\tau)-\phi(t)]}\right\}, \qquad (3.5)$$

$$C_2(\tau) = \int_{-\infty}^{\infty} dt \left\{E^2(t-\tau)E^2(t)e^{i2[\phi(t-\tau)-\phi(t)]}\right\}. \qquad (3.6)$$

The intention of writing eq.(3.3) in this form is to illustrate that the autocorrelation has three frequency components respectively centered about 0, ω_0 and $2\omega_0$. Note that the frequency mentioned here is merely the variation of $G^{(2)}(\tau)$ as a function of the delay time τ. What is interesting to note is that, given that the intensity is equal to the modulus squared of the electric field amplitude (from eq.(2.12)-dropping the coefficients), $C_0(\tau)$ can be rewritten as:

$$C_0(\tau) = \int_{-\infty}^{\infty} dt \left\{I^2(t-\tau) + I^2(t) + 4I(t-\tau)I(t)\right\}. \qquad (3.7)$$

$C_0(\tau)$, as it turns out, describes the phenomenon of second-order intensity autocorrelation (third term in integral) with background terms (first and second term in integral). $C_1(\tau)$ and $C_2(\tau)$ on the other hand basically form "interferograms" of $E(t)$ and $E^2(t)$ respectively.

3.1 Interferometric Autocorrelation

Interferometric autocorrelation (IAC) is one of the most frequently used pulse characterization techniques. It is generally used to determine pulse durations $\Delta\tau$ and temporal phase modulations $\phi(t)$. An interesting feature of the second-order IAC expression eq.(3.3) is that there exists a fixed peak to background ratio. This ratio is obtained as follows: $G^{(2)}(\tau)$ has its maximum peak value when there is no time delay ($\tau = 0$) between $E(t)$ and $E(t - \tau)$, thus $G_{peak} = G^{(2)}(0) = 16 \int_{-\infty}^{\infty} E^4(t) dt$. The background is obtained when the time delay between $E(t)$ and $E(t-\tau)$ is such that no correlation occurs, this happens when $\tau = \infty$ which results in a background of $G_{back} = G^{(2)}(\infty) = 2 \int_{-\infty}^{\infty} E^4(t) dt$. Consequently, the peak to background ratio for IAC is $8 : 1$.

Another characteristic of the IAC function, is the inherent time ambiguity which stems from the fact that second order processes are all symmetric in time. Time ambiguity is established through simply changing variables in eq.(3.1); by letting $t' = t - \tau$:

$$
\begin{aligned}
G^{(2)}(\tau) &= \int_{-\infty}^{\infty} \left| [\mathcal{E}(t) + \mathcal{E}(t - \tau)]^2 \right|^2 dt \\
&= \int_{-\infty}^{\infty} \left| [\mathcal{E}(t' + \tau) + \mathcal{E}(t')]^2 \right|^2 dt' \\
&= G^{(2)}(-\tau).
\end{aligned}
\tag{3.8}
$$

In order to determine the characteristics of a laser pulse, consider the example of a linearly chirped Gaussian pulse described in section 2.2.2 as:

$$
E(t) = A_0 \exp\left\{ -2\ln 2 \left[1 + ib_0\right] \left(\frac{t}{\Delta\tau}\right)^2 \right\}
\tag{3.9}
$$

where A_0 is the amplitude, $\Delta\tau$ with pulse width and b_0 the linear chirp parameter. The IAC for this pulse can be computed analytically:

$$
\begin{aligned}
G^{(2)}(\tau) &= A_0^4 \Bigg\{ 1 + 2\exp\left\{ -2\ln 2 \left(\tfrac{\tau}{\Delta\tau}\right)^2 \right\} \\
&+ 4\exp\left\{ -2\ln 2 \left[\tfrac{b_0^2+3}{4}\right] \left(\tfrac{\tau}{\Delta\tau}\right)^2 \right\} \cos\left(b_0 \ln 2 \left(\tfrac{\tau}{\Delta\tau}\right)^2\right) \cos\left(\omega_0 \tau\right) \\
&+ \exp\left\{ -2\ln 2 \left[1 + b_0^2\right] \left(\tfrac{\tau}{\Delta\tau}\right)^2 \right\} \cos\left(2\omega_0 \tau\right) \Bigg\}.
\end{aligned}
\tag{3.10}
$$

Eq.(3.10) includes all the parameters ($\Delta\tau$, b_0, ω_0) required to characterize the laser pulse in the time domain. The second-order IAC signal mentioned above for an unchirped ($b_0 = 0$) Gaussian pulse is graphically illustrated in fig.(3.1). What might not be clear on fig.(3.1(a)), is the fringe pattern which

(a) Full time signal.   (b) When zoomed in.
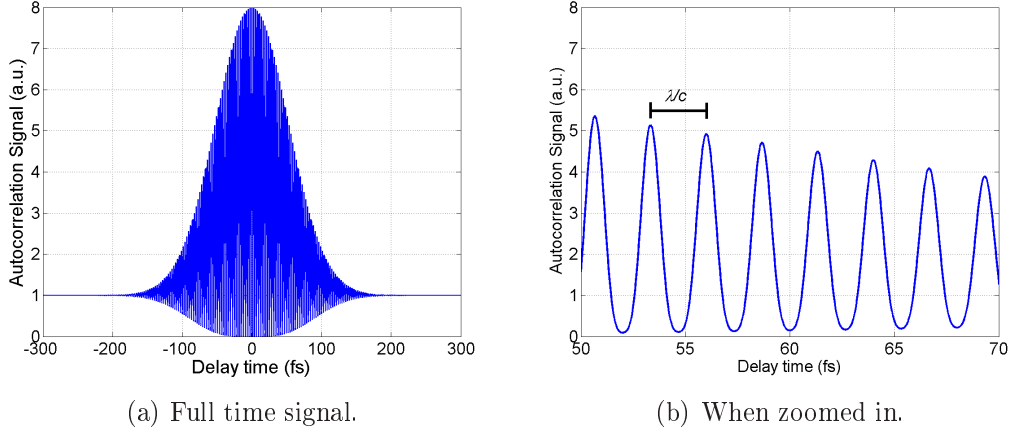
Figure 3.1: Calculated IAC signal for a 80fs Gaussian laser pulse centered at 800 nm with zero chirp ($b_0 = 0$).

is clearly visible on fig.(3.1(b)) when zooming in. These consecutive peaks and valleys correspond to constructive and destructive interference of the pulse with its time-delayed copy. Therefore, successive peaks (or valleys) will be separated by an optical path-difference which is equal to the wavelength λ of laser pulse electric field divided by the speed of light in a vacuum c. The generated interference pattern (in fig.(3.1(a))) is very sensitive to any phase distortions in the laser pulse, as can be seen for a chirped Gaussian pulse in fig.(3.2(a)) where the fringes are diminished at the flanks with even a pedestal forming at the bottom. The effect of pedestal formation for increasing chirp values is shown more clearly when looking only at the envelope functions of the IAC signal in fig.(3.2(b)). These envelopes were obtained by simply setting $\omega_0\tau$ equal to 0 for the upper envelope and π for the lower envelope.
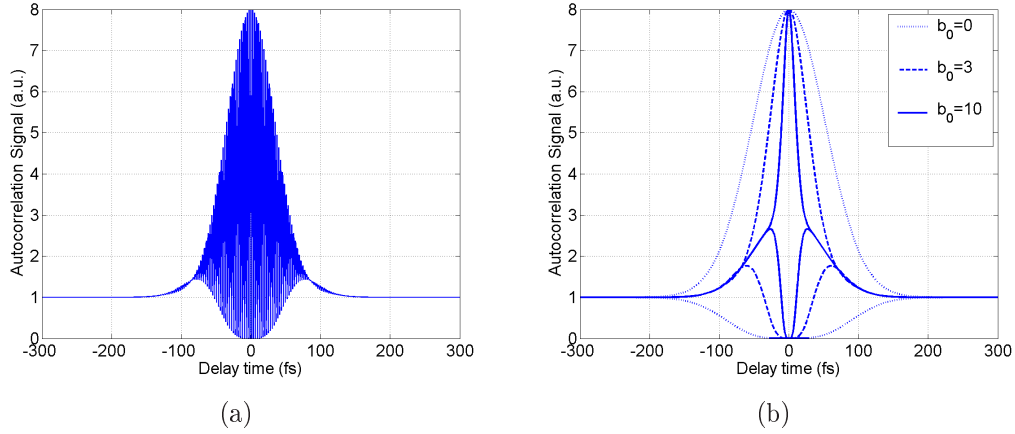
Figure 3.2: Calculated IAC: (a) signal for a 80 fs Gaussian laser pulse with chirp ($b_0 = 2$), (b) upper and lower envelopes for different chirp values.

3.2 Modified Spectrum Auto-interferometric Correlation

Modified spectrum auto-interferometric correlation (MOSAIC) is a pulse characterization technique developed by Hirayama et al in 2002 [14]. This technique merely modifies the IAC making it more sensitive to temporal chirp. The modification is done through spectral filtering and reshaping of the second-order IAC signal. A MOSAIC trace is generated by firstly Fourier transforming the IAC trace in eq.(3.3), then eliminating the ω_0 term and amplifying the $2\omega_0$ term by a factor of 2 before taking the inverse Fourier transform which results in:

$$G_{MOSAIC}^{(2)}(\tau) = C_0(\tau) + \Re\left\{4C_2(\tau)e^{i2\omega_0\tau}\right\}. \qquad (3.11)$$

The reason for considering only the $2\omega_0$ term is because it contains temporal chirp information ($2\left[\phi(t-\tau) - \phi(t)\right]$) which is twice as pronounced as that of the ω_0 term. Amplification by a factor of 2 merely secures that $G_{MOSAIC}^{(2)}(\tau)$ has a flat baseline when there is no chirp present, i.e. $\phi(t-\tau) - \phi(t) = 0$.
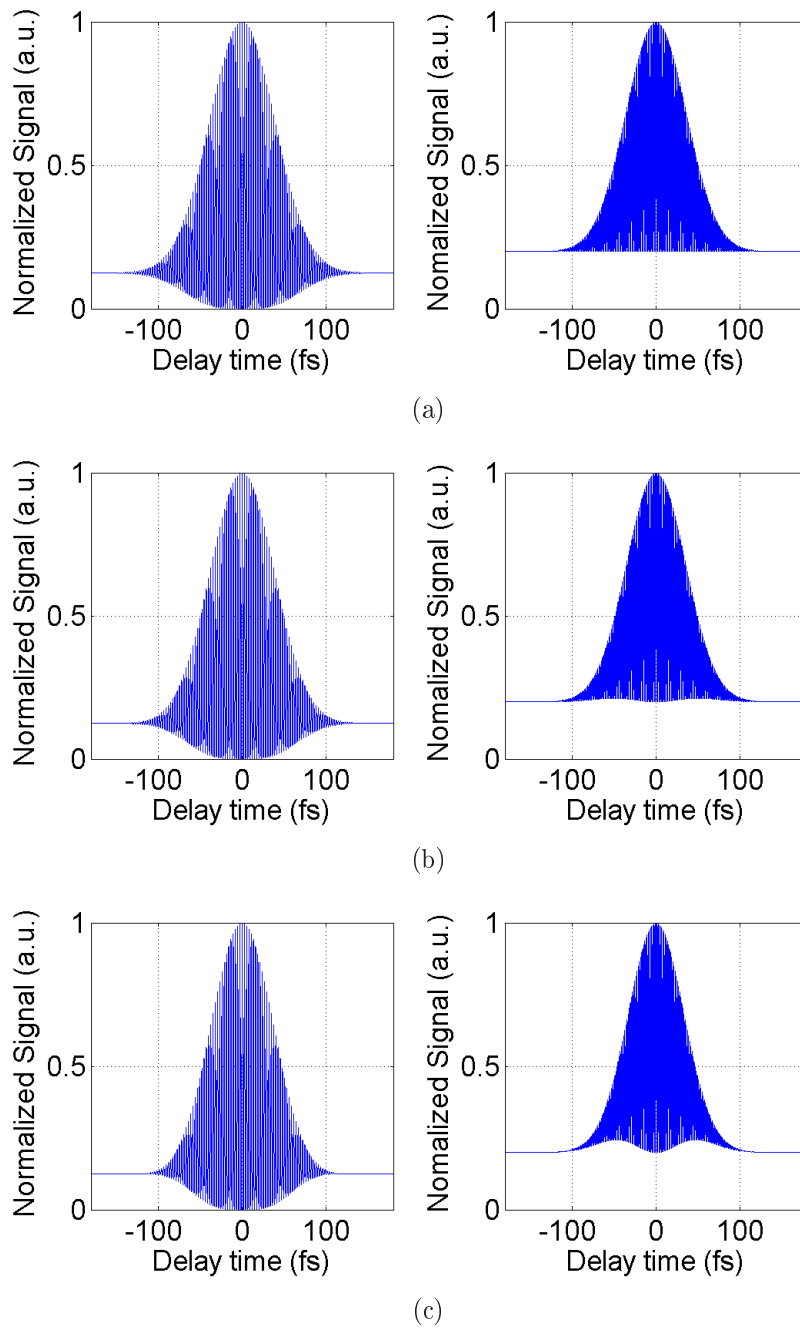
Figure 3.3: Calculated IAC (left) and MOSAIC (right) traces for 60fs Gaussian pulse with linear chirp values of; (a) $b_0 = 0$ (unchirped), (b) $b_0 = 0.3$, (c) $b_0 = 0.6$.

The sensitivity of MOSAIC to small chirp values is demonstrated in fig.(3.3) with the use of the linearly chirped Gaussian pulse given by eq.(3.9). As expected, in the case of zero chirp the MOSAIC trace shows a flat baseline. However, when the pulse is chirped, a double-bump pedestal appears which increases with the value of the chirp parameter b_0. From fig.(3.3) it should also be noted that there appear to be no visible changes in the calculated IAC traces for the various chirp parameters.

3.3 Background-free Autocorrelation

Background-free autocorrelation (BFA) is an IntenAC pulse characterization technique only capable of determining the pulse width $\Delta\tau$. BFA, as the name suggests, is merely the normal second-order intensity autocorrelation (as described in eq.(3.7)) without any background contribution. Therefore the BFA signal can be expressed as follows:

$$G_{BFA}^{(2)}(\tau) = \int_{-\infty}^{\infty} I(t-\tau)I(t)dt. \tag{3.12}$$

It is important to note however, that it is impossible to extract any phase information from $G_{BFA}^{(2)}(\tau)$, because phase information is lost when considering intensities only. The ability of BFA to only determine pulse durations, becomes apparent when rewriting eq.(3.12) for the Gaussian pulse described in eq.(3.9),

$$G_{BFA}^{(2)}(\tau) = A_0^4 \exp\left\{-2\ln 2\left(\frac{\tau}{\Delta\tau}\right)^2\right\} \tag{3.13}$$

where $\Delta\tau$ is the pulse duration. The FWHM of the BFA signal in eq.(3.13) can be obtained through the procedure explained in section 2.2.2 since,

$$\Delta\tau_{BFA} = \sqrt{2}\Delta\tau \tag{3.14}$$

which just underlines the relation between the FWHM of the pulse and that of the BFA signal. Table 3.1 taken form Vasil'ev et al [26] summarizes BFA traces (graphically illustrated in fig.(3.4)) and FWHM relations for the pulse

profiles shown in table 2.1 where the pulse parameter a was taken as one.

Pulse profile:	Normalized $G_{BFA}^{(2)}(\tau)$	$\Delta\tau_{BFA}/\Delta\tau$
Gaussian	$\exp\left(-\tau^2/2\right)$	1.4142
Sech	$\frac{3[\tau\coth(\tau)-1]}{\sinh^2(\tau)}$	1.5427
Lorentzian	$\left[1+(\tau/2)^2\right]^{-1}$	2
Two-sided exponential	$\left[1+2\left|\tau\right|\right]\exp\left(-2\left|\tau\right|\right)$	2.4213

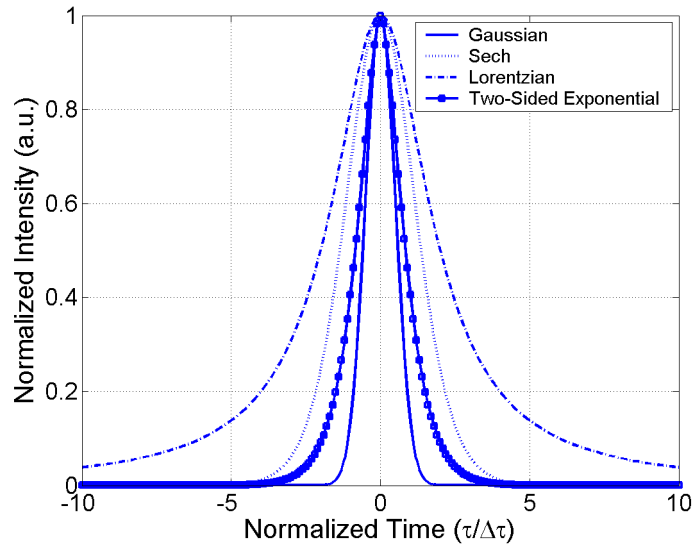Table 3.1: Second-order autocorrelation functions for various pulse shapes.

Figure 3.4: BFA traces for various pulse profiles.

3.4 Frequency Resolved Optical Gating

Frequency resolved optical gating (FROG) is a pulse characterization technique, which allows for full pulse characterization in both the time and frequency domain. That is, FROG is capable of determining the temporal intensity $I(t)$, the spectral intensity $S(\omega)$, the pulse width $\Delta\tau$, the temporal phase $\phi(t)$, the spectral width $\Delta\omega$ and the spectral phase $\varphi(\omega)$. The basis of FROG is similar to the above mentioned techniques, where a pulse is allowed to interact with a time delayed copy of itself. The only difference is that the autocorrelation signal is now recorded in both the time and frequency domain. There exist various types of FROG techniques which depend merely on the type of interaction between the pulse and its copy. In this section the second-order FROG also called SHG FROG will be studied. The most general expression of a SHG FROG trace is:

$$I_{FROG}^{SHG}(\omega, \tau) = \left| \int_{-\infty}^{\infty} E_{sig}(t, \tau) e^{-i\omega t} dt \right|^2 \tag{3.15}$$

where $E_{sig}(t, \tau)$ is the signal field which is proportional to the second-order nonlinear polarization $P_{2\omega}^{NL}(t, \tau) = 2\chi^{(2)}\mathcal{E}(t - \tau)\mathcal{E}(t)$. For SHG FROG, the signal field is defined as:

$$E_{sig}(t, \tau) = \mathcal{E}(t - \tau)\mathcal{E}(t). \tag{3.16}$$

The expression for the SHG FROG trace in eq.(3.15) is clearly the intensity (modulus squared) of the Fourier transform of the signal field, which explains the terms "frequency resolved" in the acronym FROG, whilst the meaning of the terms "optical gating" becomes clear when considering that the time delayed laser pulse copy $\mathcal{E}(t-\tau)$ is essentially a gate pulse, which "gates" the information of the probe pulse $\mathcal{E}(t)$.

The SHG FROG trace for a 100 fs Gaussian pulse centered at 800 nm (eq.(3.9)) is graphically depicted in fig.(3.5). Fig.(3.5) clearly shows how the FROG trace broadens in the wavelength (or frequency) domain for a chirped pulse. Also take note that the FROG trace is truly a SH signal
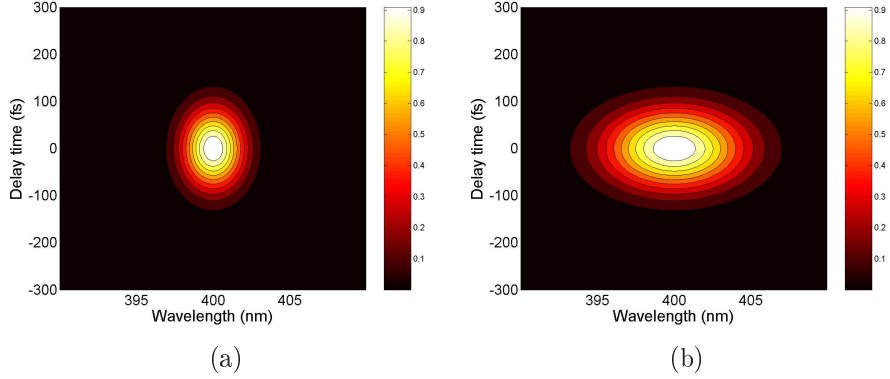
Figure 3.5: Calculated SHG FROG trace of a (a) unchirped and (b) chirped ($b_0 = 2$) 100 fs Gaussian pulse centered at 800 nm.

because it is centered at 400 nm.
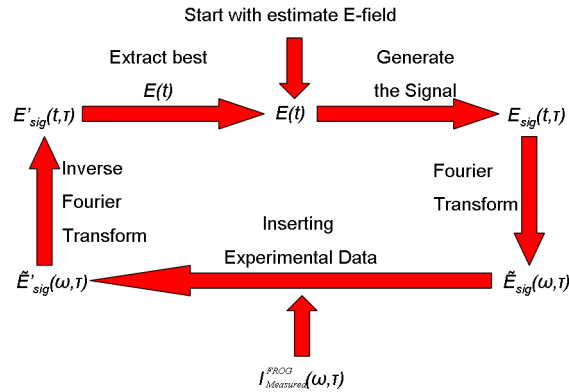
Figure 3.6: FROG Algorithm.

In order to understand how FROG is capable of complete pulse characterization, assume that an experimental setup exist which measured a certain SHG FROG trace, say $I_{Measured}^{FROG}(\omega, \tau)$. The characteristics of the experimental laser pulse which results in $I_{Measured}^{FROG}(\omega, \tau)$, is then determined through a Fourier algorithm (shown in fig.(3.6)). This algorithm is an iterative process which works as follows: Starting with an initial estimate for the field $\mathcal{E}(t)$, a signal field is generated $E_{sig}(t, \tau)$ according to eq.(3.16). The Fourier transform of the signal field $\tilde{E}_{sig}(\omega, \tau)$ is then calculated. The amplitude of the

signal field is then replaced by $\sqrt{I_{Measured}^{FROG}(\omega, \tau)}$, creating a new signal field $\tilde{E}'_{sig}(\omega, \tau)$ with a better amplitude estimation:

$$\tilde{E}'_{sig}(\omega, \tau) = \frac{\tilde{E}_{sig}(\omega, \tau)}{\left|\tilde{E}_{sig}(\omega, \tau)\right|} \sqrt{I_{Measured}^{FROG}(\omega, \tau)} \qquad (3.17)$$

Note however that no adjustment in phase is made in this step. The next step calculates the inverse Fourier transform of $\tilde{E}'_{sig}(\omega, \tau)$, transforming it back into the time domain as $\tilde{E}'_{sig}(t, \tau)$. The last step in the cycle generates a new electric field $\mathcal{E}'(t)$ from the modified signal field $\tilde{E}'_{sig}(t, \tau)$ by simple integration over the delay time τ:

$$\mathcal{E}'(t) = \int_{-\infty}^{\infty} \tilde{E}'_{sig}(t, \tau) d\tau. \qquad (3.18)$$

From this new electric field $\mathcal{E}'(t)$, a retrieved FROG trace $I'_{FROG}(\omega, \tau)$ is then calculated which is compared to the experimental FROG trace $I_{Measured}^{FROG}(\omega, \tau)$, by means of an error calculation. This step completes the algorithm, which is then repeated until the error is sufficiently minimized. The estimate $\mathcal{E}'(t)$ resulting in a optimally minimized error is then the fully characterized retrieved pulse.

Chapter 4

Experimental Setups

Chapter 2 dealt with the theoretical description of laser pulses, more specifically it was shown that a pulse traveling through a medium with high GVD will eventually be broadened. It was also shown that if a pulse were to propagate through a NLO medium, with a large value for $\chi^{(2)}$, SHG can occur when properly phase-matched. In this chapter, SHG or more generally second-order processes will be exploited to design experimental setups capable of pulse characterization through the techniques mentioned in Chapter 3. The experimental setup for MOSAIC is identical to that of IAC, and for that reason will not be discussed.

In order to design any pulse characterization technique, some information about the pulse is required. This information includes a rough estimate of the pulse-width regime (fs or ps), the spectral bandwidth $\Delta\lambda$ and central wavelength λ_0 (or frequency), the repetition rate f_{rep} and the pulse energy E_{pulse}. For this purpose, the laser systems which emit these (yet to be characterized) pulses will be discussed next.

4.1   The Laser Systems

The first system that will be characterized is a commercially available fs oscillator, called the Tsunami Mode-Locked Ti:Sapphire Laser. The Tsunami

is optically pumped by a 5.5 W diode-pumped cw neodymium yttrium vana-date (Nd:YVO$_4$) solid state laser, named Millennia Vs. The Millennia Vs uses Nd:YVO$_4$ as gain medium which delivers with high efficiency, near infra-red (NIR) radiation which is frequency doubled within the cavity by a lithium triborate (LBO) crystal to a emission wavelength of 532 nm. Both the Tsunami and Millennia Vs were designed and manufactured by Spectra-Physics [27, 28].

The Tsunami is an example of a fs laser in which both active and passive mode-locking techniques are applied in order to produce stable fs laser pulses. Passive mode-locking is obtained through KLM (as discussed in section 2.1) which is a non self-starting technique, whilst active mode-locking is achieved by inserting an acoustic optic modulator (AOM) into the laser cavity close to an end mirror. The AOM is a loss modulator which comprises of a high quality quartz crystal with two polished surfaces which are parallel to the intra-cavity beam direction. One of these surfaces is attached to a piezo-electric transducer which is driven at a rf frequency generating an acoustic wave within the quartz medium (fig.(4.1(a))). Reflection from the opposite polished surface, now generates a standing acoustic wave within the quartz crystal. This standing wave induces a time-dependent refractive index grating with a modulation amplitude of $2\Delta_m$ along an axis perpendicular to the light direction (fig.(4.1(b))). Therefore, as light passes through the grating, a fraction of it is diffracted and frequency-shifted by an amount equal to the acoustic frequency ω_{AOM}. Upon reflection from the cavity end mirror, the diffracted and undiffracted rays pass through the modulator once again, resulting in a portion of each of the two beams being diffracted. This means that for a rf drive frequency of ω_{AOM}, the generated acoustic grating will switch on and off at a rate equal to $2\omega_{AOM}$.

The AOM thus acts like a time-dependent loss modulator, because it only diffracts light out of the laser cavity when the time-dependent grating is present. Fig.(4.1(c)) shows how in the frequency domain this loss modula-tion imparts modulated sidebands when a wave passes through the AOM. Now, seeing that the frequency spacing Δf between consecutive longitudinal
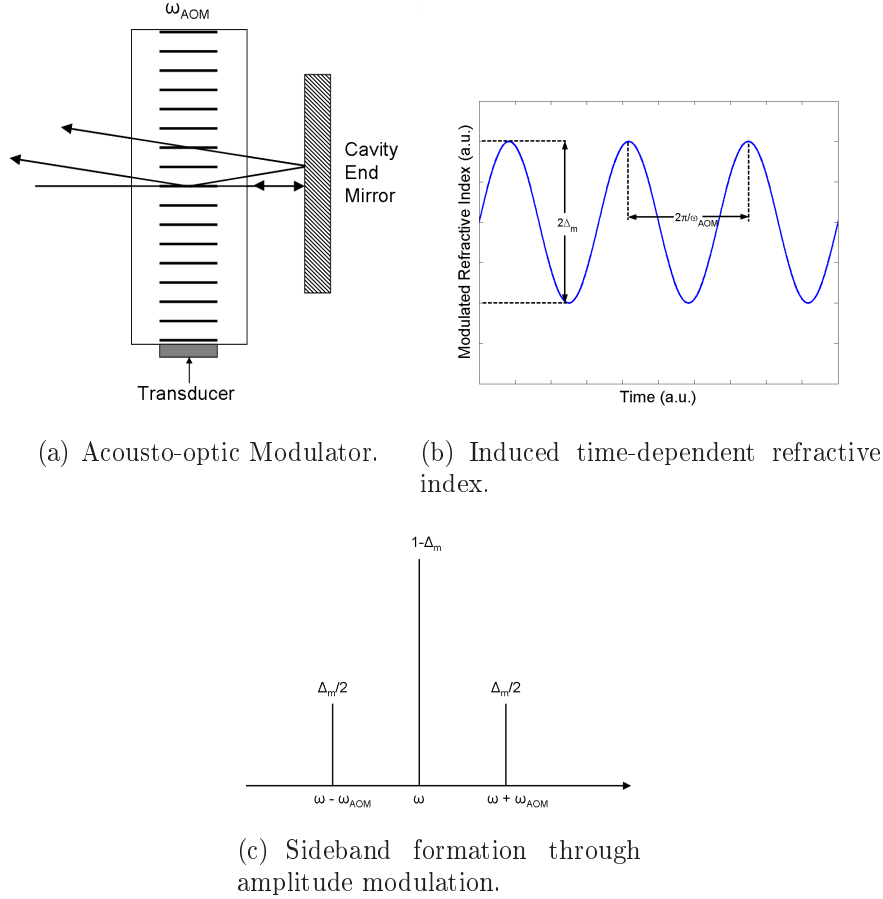
(a) Acousto-optic Modulator.

(b) Induced time-dependent refractive index.

(c) Sideband formation through amplitude modulation.

Figure 4.1: Active mode-locking using an AOM.

cavity modes is related to the cavity length L, as $\Delta f = c/2L$ where c is the speed of light in a vacuum. If the acoustic frequency ω_{AOM} is chosen such that $2\omega_{AOM} = \Delta f$, the sidebands generated by the AOM will then overlap with the longitudinal cavity modes centered at $\omega - \omega_{AOM}$ and $\omega + \omega_{AOM}$ respectively, resulting in a type of phase communication between consecutive cavity modes. This phase communication is the basic requirement for mode-locking, giving rise to active mode-locking [29, 28].

As a final point, the active mode-locking technique applied in the Tsunami, merely secures that mode-locking is initially established and stabilized, whereas passive KLM in the Tsunami ensures that the fs pulse generated initially

Peak Wavelength (λ_0):	790 nm
Average Power (P_{ave}): with 6 W TEM$_{00}$ pump	0.5 mW
Peak Power (P_{peak}): with 6 W TEM$_{00}$ pump	> 75 kW
Pulse Width ($\Delta\tau$):	< 80 fs
Tuning range (nm): with 6 W TEM$_{00}$ pump	$735 - 840$
Repetition rate (f_{rep}):	82 MHz

Table 4.1: Tsunami specifications.

through the insertion of an AOM has indeed the highest intensity[1]. Table 4.1 lists the Tsunami specifications for a peak wavelength of $\lambda_0 = 790$ nm [28].

The next system that required characterization, was a chirped pulse amplification system called Alpha-1000 S (B.M. Industries), which was used to amplify the pulses emitted by the Tsunami. The Alpha-1000 S consists of three distinct parts; a pulse stretcher, a regenerative amplifier pumped by a Nd:YAG laser (Continuum) and a pulse compressor [30, 31]. These components are used in such a way as to amplify the fs input pulse without causing damage to any optical components within the system itself. The method of amplification can be described as follows (depicted in fig.(4.2)): the fs pulse is firstly sent to a pulse stretcher where it experiences positive GVD which effectively lowers the peak power; this stretched pulse then passes through a regenerative amplifier which increases the pulse energy; finally the high energy stretched pulse is compressed by allowing it to experience negative GVD.
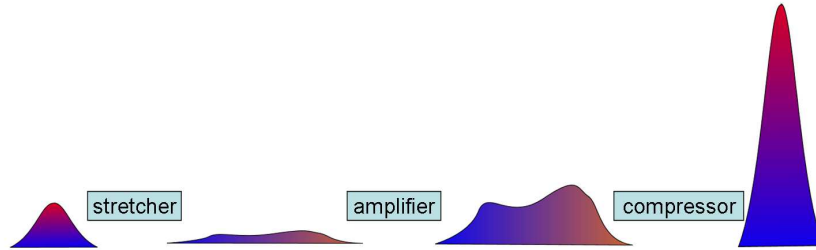
---

[1]Refer back to section 2.1.

Figure 4.2: The principle of chirped pulse amplification.

The principle of pulse stretching as mentioned above, is to impart positive GVD onto a pulse. This means that the red spectral components of a laser pulse moving through a medium (or an optical system) with positive GVD effectively have a shorter optical path length then the blue spectral components. Positive GVD is generally introduced into a pulse, by the specific arrangement of diffraction gratings and lenses shown in fig.(4.3). Take note
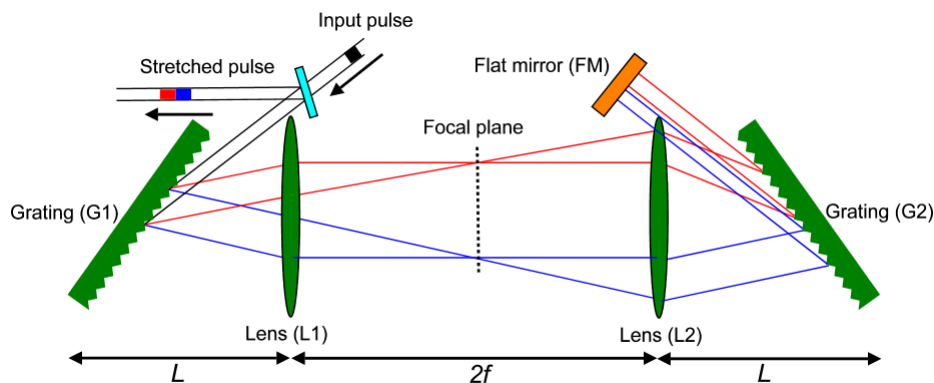
Figure 4.3: Schematic layout of a grating based pulse stretcher.

that pulse stretching through positive dispersion (as depicted in fig.(4.3)) requires that the distance L should be shorter then the focal length f. For $L > f$, negative dispersion results and for $L = f$ no dispersion is imparted on the pulse. The pulse stretcher setup in the Alpha-1000 S is however, slightly different from the one in fig.(4.3). The differences are that a focusing mirror instead of the lens (L1 in fig.(4.3)) is used, and a flat mirror is inserted at the focal plane of L1. This greatly simplify the elaborate telescope-like setup in fig.(4.3).

The amplification of the stretched pulses occurs in a Ti:Sapphire laser cavity. Ti:Sapphire crystal as gain medium was used because of its broad emission spectrum. The laser gain medium is optically pumped by a 532 nm, 20 Hz flashlamp-pumped Nd:YAG laser. When the stretched pulse enters the cavity and moves through the laser medium, the gain within the Ti:Sapphire crystal is extracted leading to pulse amplification. Note that gain is extracted on every round-trip of the pulse within the cavity. When sufficient pulse amplification is obtained, the pulse is then actively switched out of the cavity.

The amplified stretched pulse is then compressed by allowing the pulse to move through an optical setup with negative GVD. The compressor setup
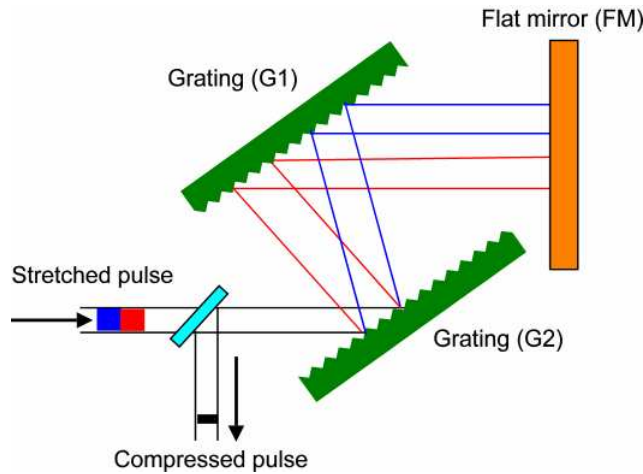
Figure 4.4: Schematic layout of a grating based compressor.

shown in fig.(4.4) uses a grating system similar to that of the stretcher (fig.(4.3)). The geometry of the gratings for pulse compression is designed such that the blue spectral component of the stretched pulse has a shorter optical path length than the red spectral components (i.e. imparts negative GVD). Bare in mind however that again the compressor design in fig.(4.4) is not identical to the designed used in the Alpha-1000 S system although the principle is the same.

In conclusion it is expected for the fully optimized regenerative amplifier system to emit fs pulses at a low repetition rate (20 Hz pump) with increased pulse energies (micro- (μJ) to mili-Joules (mJ)). Knowing that the pulses

emitted by the Tsunami reach pulse energies of only a couple of nano-Joules (nJ), this means that pulse amplification with a factor of $\times 100000$ is ultimately achievable with the Alpha-1000 S system.

4.2 Interferometric Autocorrelation

4.2.1 IAC System Layout

The design of an IAC experimental setup must ensure that the restrictions, like the second-order condition and the interaction of the pulse with a time-delayed copy of itself in eq.(3.1), are obeyed. Fig.(4.5) shows the experimental setup for IAC previously designed by Scheidt [17]. This custom built autocorrelator is based on rapid-scan Michelson interferometer (fig.(4.5)). The
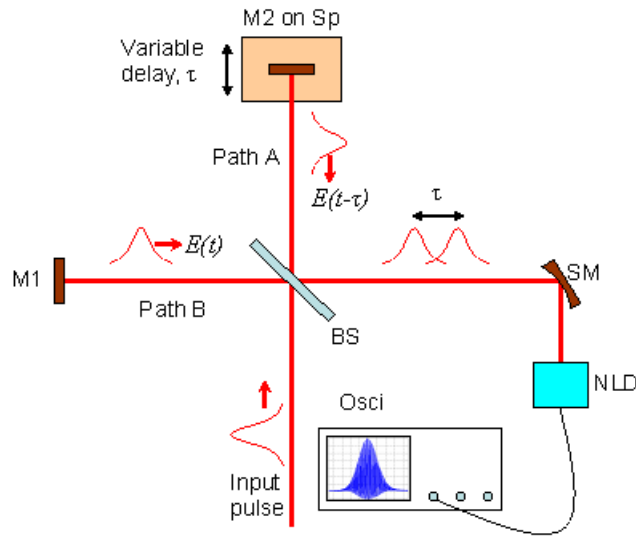

Figure 4.5: IAC setup. BS: 50/50 beam splitter, M1, M2: Au coated mirrors, Sp: speaker, τ: temporal delay, SM: spherical Au coated mirror, NLD: Non-linear detector, Osci: Oscilloscope.

input laser beam is split by a 50/50 dielectric beam splitter (BS) mounted at an angle of 45°, into two parts which are then sent to mirrors M1 and

M2 where they are reflected onto themselves. M2 is mounted on an audio speaker which is driven with a sinusoidally modulated voltage, with a chosen amplitude and frequency. The movement of the speaker together with M2 causes a varying optical path-length difference Δx in path A which ultimately leads to a temporal delay of $\tau = 2\Delta x/c$, where c is the speed of light, between the two laser pulse copies $E(t)$ and $E(t - \tau)$. These pulse copies are then spatially superimposed by the BS and focused by the spherical mirror (SM) onto a second-order non-linear detector (NLD). In order to generate a signal equivalent to eq.(3.1) the detector should be restricted to SHG detection (as described in section 2.3.3.1). Therefore it is advisable to make use of collinear SHG in a NLO crystal. However, the only prerequisite of the detector is that it should be able to detect a second-order signal at a higher frequency than the speaker oscillation. The alternative then, is to use the phenomenon of two photon absorption (2PA) in a suitable reversed biased light emitting diode (LED). In this setup an AlGaAs-diode, with a band gap energy E_{bg} of about 1.9 eV, is used for second-order detection. The reason why this LED favours second-order detection, is because the incident laser beam has a peak wavelength of 800 nm, or single photon energy of $E_p = 1.55$ eV which is not enough to excite electrons across E_{bg}. Linear absorption will therefore not occur but 2PA is expected. A signal due to 2PA in the LED is then generated simply because the input laser radiation intensity is adequate enough (increasing the probability of 2PA) and that the energy of 2PA is equal to a photon energy of $2E_p$ which is significantly larger then E_{bg}. Therefore, the 2PA signal resulting from optical excitation of an electron in the LED valence band to the conduction band, generally referred to as light induced electric current (photo-current), is monitored on the oscilloscope (Osci).

4.2.2 IAC System Optimization

Sensible conclusions from an IAC signal can only be made if the measured IAC trace is recorded using a non-linear detector, which is limited to second-order detection. This means that (similar to eq.(2.82)), the detected pho-

tocurrent signal S_{PC}, should vary quadratically with the increase of the incident fundamental intensity I_ω. Fig.(4.6) shows that the AlGaAs-diode
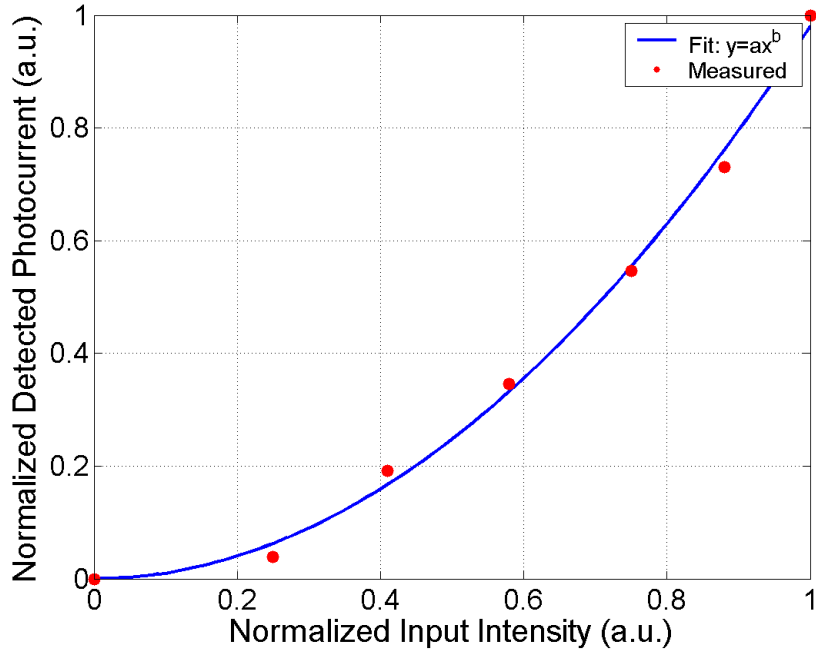
Figure 4.6: Measured photocurrent signal (solid line) vs normalized input intensity of the AlGaAs-diode. A quadratic fit (dots) on the measured signal yields; $a \approx 0.98 \pm 0.01$, $b \approx 1.98 \pm 0.08$.

as detection instrument gives the appropriate quadratic response to varying input intensities, because $b \approx 2$ implies that $S_{PC} \propto (I_\omega)^2$. The fit shown in fig.(4.6) was done through by least square method which applies the Levenberg-Marquardt algorithm.

Alignment of the IAC system is also extremely critical, because any misalignment results in an unwanted IAC trace where the $8:1$ ratio or the required symmetry (as discussed in section 3.1) is not achieved. This occurs when the overlapping pulses are not completely collinear.

4.3 Background-free Autocorrelation

An experimental setup for BFA measurements should be capable of generating experimental traces which are proportional to eq.(3.12). Experimental traces should in other words only come from the autocorrelation of the pulse intensity $I(t)$ which excludes all background contributions. The custom-made BFA setup developed as part of this work is described below.

4.3.1 BFA System Layout

As shown in fig.(4.7), the input pulse is divided by a 50/50 dielectric beam splitter (BS) mounted at an angle of 45° into two paths A and B. The pulse copy in path B is reflected onto itself from mirror M1 which is mounted on a linear translation stage (TS). Similar to the speaker in fig.(4.5), TS is responsible for creating a temporal delay τ between the pulse copies $I(t)$ and $I(t - \tau)$. In path A however, the pulse copy $I(t)$ is sent to a set of perpendicular arranged mirrors (M2 and M3), which results in the reflected pulse being horizontally displaced. A portion of the reflected pulse from path B then moves through the BS and is focused together with a portion of the reflected pulse from path A into a thin β-Barium Borate (BaB$_2$O$_4$ or BBO) crystal. Note that due to the horizontal displacement of the pulse copy in path A, focusing into the BBO crystal is non-collinear. When aligned properly, this non-collinear arrangement of input pulses on a NLO crystal such as BBO, results in SH light being generated in the forward direction. Due to this non-collinear setup, the input pulse copies are easily spatially filtered after their interaction within the NLO crystal,by using an iris (A). This means that the generated SH light in the forward direction, is free of any contributions from $I(t)$ or $I(t - \tau)$ individually (background-free). The generated SH signal is then reflected off a dielectric mirror (F1) which is highly reflective for 400 nm light and anti-reflective for 800 nm light at an incident angle of 45°, then it passes through neutral density filters (F2) and is detected by a photo-multiplier tube (PMT). F1 is merely used to filter out any scattered fundamental light (800 nm), whilst F2 is used for attenuation.
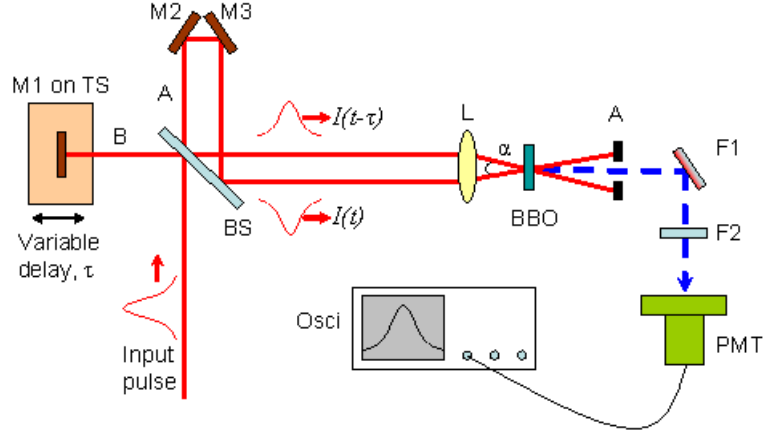
Figure 4.7: BFA setup. BS: 50/50 Beam splitter, M1, M2, M3: Au coated mirrors, TS: Linear translation stage, τ: Temporal delay, L: Lens, α: Angle between input pulse, BBO: β-Barium Borate crystal, A: Iris as variable aperture, F1: Dielectric mirror-HR 400 nm & AR 800 nm incident at 45°, F2: Neutral density filters, PMT: Photo-multiplier tube, Osci: Oscilloscope.

The signal generated at the PMT is then monitored on an oscilloscope (Osci) as a function of delay time τ (i.e. as the translation stage is scanned).

4.3.2   BFA System Optimization

As mentioned above, second-order detection in the BFA system is achieved through SHG in a negative uniaxial BBO crystal. BBO is chosen, because it has a large phase-matchable wavelength region (409.6-3500 nm) which makes it ideal for SHG of broad-spectrum fs pulses [32]. However, the generation of SH light in the forward direction (fig.(4.7)), will only occur if the setup is properly aligned. Alignment in this setup is extremely crucial, especially when focusing into the BBO crystal. This is because phase-matching in this case is non-collinear. To obtain type I phase-matching in BBO for the geometry in fig.(4.7) the perfectly phase-matched condition in eq.(2.85) changes to,

$$n_e(2\omega, \theta) = n_o(\omega) \cos(\alpha/2) \tag{4.1}$$

where $n_e(2\omega, \theta)$ is the extraordinary refractive index which the SH light experience at a given phase-matching angle θ, where $n_o(\omega)$ is the ordinary refractive index which the two input fields (fig.(4.7)) experience, and where α is the angle between the two input beams. Eq.(4.1) implies that for effective SHG of 800 nm pulses with the geometry in fig.(4.7), the incident angle should be $\alpha \approx 38.5^o$ [2]. This value for the optimum incident angle in turn, acts like a new alignment condition because it can be used to determine what focal length lens would be ideal (given that the horizontal displacement of the two input pulses before the lens is fixed).
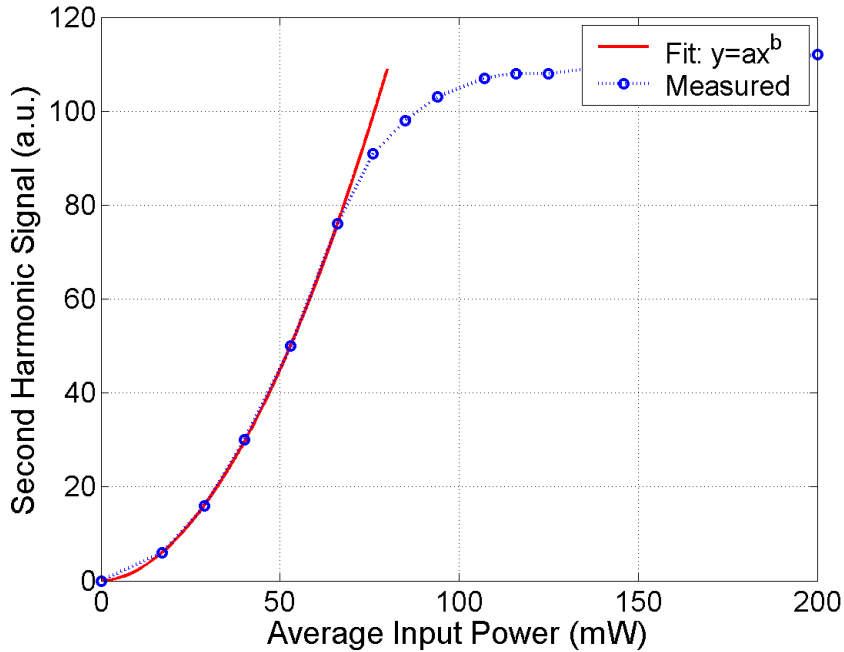
Figure 4.8: Measured second harmonic signal (dotted line with circles) vs average input power from the BBO crystal. A quadratic fit (solid line) on the first six data points of the measured signal yields; $a \approx 0.029 \pm 0.001$, $b \approx 1.878 \pm 0.012$.

When phase-matching is achieved, the next task is to determine whether the generated signal is truly a result of SHG. This is done by simply varying the

_____

[2]Note that this angle was calculated by making use of the Sellmeier's equations for BBO [32].

input power in a controlled way and monitoring the signal amplitude at Osci in fig.(4.7). The result of this verification of second-order detection is shown in fig.(4.8) where the generated signal varies quadratically with the average input power. Note that this measurement was done for maximum overlap ($\tau = 0$) between the two input pulses. In fig.(4.8) the signal monitored by the Ocsi from the PMT shows saturation at average input powers higher then 80 mW. It was determined that this saturation was due the generated signal for higher input powers, being too large for the PMT to handle. This was remedied by:

1. Using neutral density filters (F2) with higher optical densities (O.D) and/or,

2. Decreasing the supply voltage over the PMT.

Using neutral density filters with higher OD's simply attenuates the optical signal received by the PMT and thus decreasing the signal monitored by the oscilloscope. Alternatively decreasing the PMT supply voltage, decreases the PMT's amplification factor making it more insensitive to low luminosity light. This also results in a lowered signal measured at the oscilloscope.

4.4 Frequency Resolved Optical Gating Technique

A SHG FROG setup has only to record spectral data of a pulse interacting with itself within a $\chi^{(2)}$ medium. The FROG system implemented here was designed and constructed specifically for this work.

4.4.1 SHG FROG System Layout

Fig.(4.9) shows the SHG FROG setup, which is actually just a modified BFA setup. This is because instead of merely monitoring the amount of SH

generated as is done in BFA, the FROG system spectrally resolves this SH light. Similar to fig.(4.7), in fig.(4.9) an input pulse is split into two, and
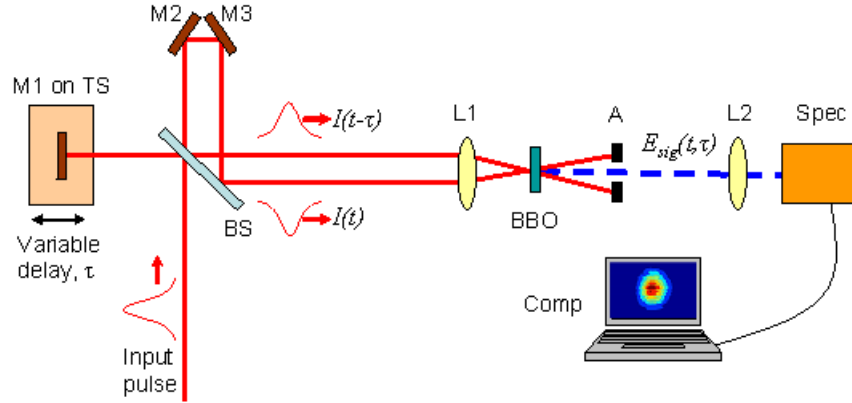

Figure 4.9: FROG setup. BS: 50/50 Beam splitter, M1, M2, M3: Au coated mirrors, TS: Linear translation stage, τ: Temporal delay, L1: Focusing Lens, BBO: β-Barium Borate crystal, A: Iris as variable aperture, L2: Focusing Lens, Spec: Spectrometer, Comp: Computer for data capture and analysis.

through various optical components these pulse copies are non-collinearly focused into a BBO crystal. For an aligned setup, SH light is generated through type I phase-matching within the BBO crystal. The SH light generated in the forward direction when the two pulse copies overlap, is then focused into a fiber-coupled spectrometer (Spec). The spectral data is then captured as a function of delay time τ by the computer (Comp). This experimentally obtained FROG trace is subsequently analyzed using commercially available FROG Algorithmic software (Femtosoft Technologies) available at femtosoft http://www.femtosoft.biz.

4.4.2 SHG FROG System Optimization

When aligning the SHG FROG setup, special care was taken when focusing the generated SH signal into the fiber-coupled spectrometer. If all the generated SH does not enter the fiber while scanning the linear translation stage (TS), it will lead to an inaccurate FROG trace. This should be avoided
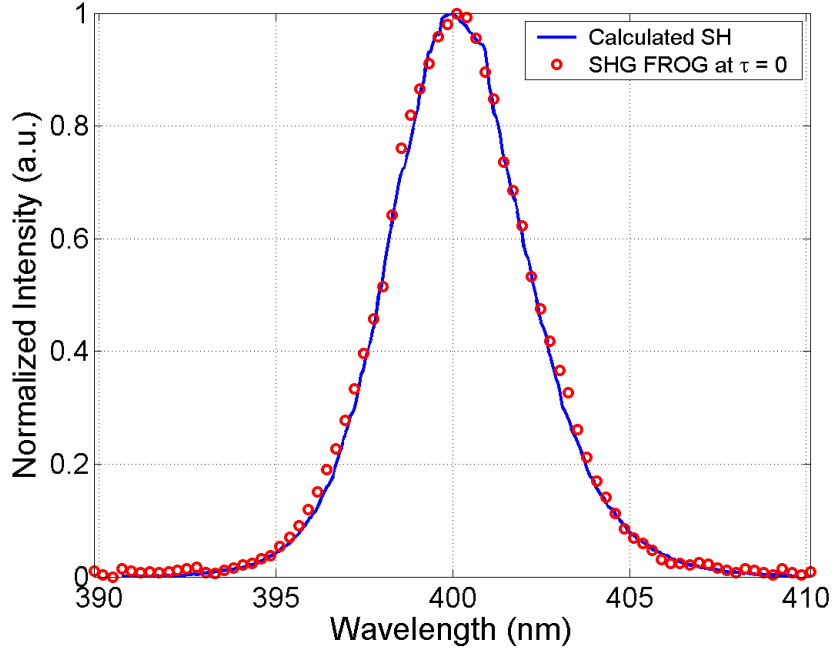
Figure 4.10: Comparison of a calculated SH spectrum trace to the FROG trace at zero delay time.

at all times, seeing that pulse reconstruction using FROG software assumes that the generated experimental trace is free from this measurement inaccuracy. Therefore, a multi-mode fiber with a diameter of 200 μm and numerical aperture (NA) of 0.22 was used to couple light into the spectrometer.

In addition to focusing all the SH light into the fiber, spectral clipping which would lead to measurement inaccuracies were limited. Spectral clipping as used here, simply means that all the components of the fundamental pulse spectrum and SH pulse spectrum should be accounted for. Verification for this is achieved by relating the calculated SH spectrum of the input pulse spectrum $S(\lambda)$ to the FROG trace $I^{FROG}_{Measured}(\lambda, \tau = 0)$ when the two pulses overlap exactly. This is because the FROG trace at zero delay time is exactly the SH spectrum of the input pulse. The calculated SH spectrum is simply determined by taking the square root of $S(\lambda)$ and plotting it over wavelengths of 2λ. This is possible because the generated SH signal at zero delay can be seen as the "product" of the input field with itself. Fig.(4.10) shows that the

calculated SH spectrum agrees well with the FROG trace at zero delay time. Therefore, based on the result in fig.(4.10), one can be assured that spectral clipping does not occur.

Chapter 5

Experimental Results

In this chapter the measurements of the various pulse characterization techniques during the course of this work are presented. The various techniques are used particularly to characterize a fs laser pulse before and after amplification. For this purpose special care was taken to measure pulse characteristics under similar conditions. The one specific condition that remained constant at all measurements, was the shape of the spectral intensity $S(\lambda)$ and peak wavelength λ_0 of the input pulse. Fig.(5.1) shows a Gaussian fit on the measured spectral intensity $S(\lambda)$ of the input fs pulse recorded with a fiber-coupled spectrometer. The parameters that were extracted using this Gaussian fit was the bandwidth $\Delta\lambda = 13.5 \pm 0.14$ nm and the peak wavelength $\lambda_0 = 800.4 \pm 0.05$ nm. The error values shown here (and in the rest of this section), are merely the 95% confidence bounds of the fitted values.

The bandwidth of the pulse in the frequency domain $\Delta\nu$ can be calculated from the expression which relates the frequency ν and the wavelength λ, $\nu = c/\lambda$. In order to do this, the derivative of the expression with respect to λ is calculated. This results in the following: $d\nu = -c/\lambda^2 d\lambda$, where $d\nu$ can be seen as the frequency bandwidth, where $d\lambda$ is the wavelength bandwidth and λ^2 the square of the peak wavelength. Taking all of this into account and also dropping the minus in the derivative, the frequency bandwidth of the fs pulse under investigation is calculated to be $\Delta\nu = 6.34$ THz.
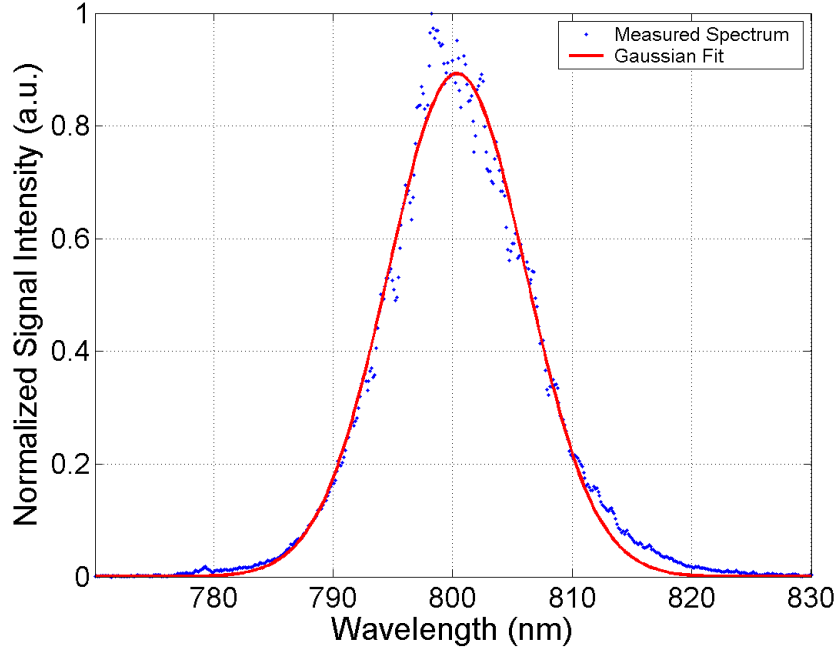
Figure 5.1: Tsunami measured (dots) spectral intensity together with its Gaussian fit (line).

The first set of measurements shows the results obtained for IAC, MOSAIC, BFA and SHG FROG measurements of the Tsunami pulse. The second set of measurements only includes the characterization of the amplified pulse through BFA and SHG FROG techniques.

5.1 Characterization of the Tsunami pulse

5.1.1 IAC results

Fig.(5.2 (a)) shows the IAC trace for the Tsunami pulse measured at 3 meters from the laser output. The positive and negative peaks of fig.(5.2 (a)) are then extracted, fitted using the envelopes of eq.(3.10) and plotted in fig.(5.2

(b)). The expressions used for fitting are;

$$
\begin{aligned}
G_{\pm}^{IAC}(\tau) \;=\;& A_0^4 \left\{ 1 + 2\exp\left\{-2\ln 2\left(\tfrac{\tau}{\Delta\tau}\right)^2\right\} \right. \\
\pm\;& 4\exp\left\{-2\ln 2\left[\tfrac{b_0^2+3}{4}\right]\left(\tfrac{\tau}{\Delta\tau}\right)^2\right\}\cos\left(b_0\ln 2\left(\tfrac{\tau}{\Delta\tau}\right)^2\right) \\
+\;& \left. \exp\left\{-2\ln 2\left[1+b_0^2\right]\left(\tfrac{\tau}{\Delta\tau}\right)^2\right\}\right\},
\end{aligned} \qquad (5.1)
$$

where '+' denotes the upper and '−' the lower envelopes of the IAC fit for a linearly chirped Gaussian pulse. The results for the fitting parameters obtained from the upper and lower envelope in fig.(5.2 (b)) did not match exactly. The same fitting procedure was applied to the trace in fig.(5.3 (a)).
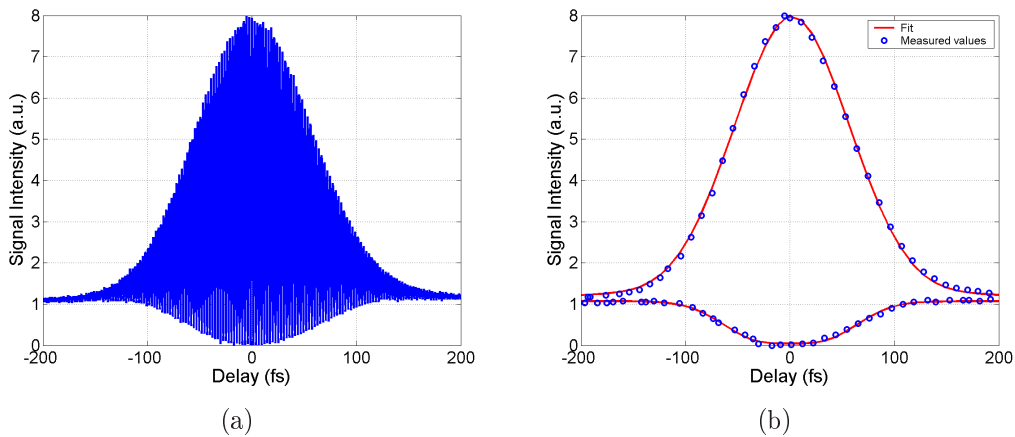
Figure 5.2: Measured IAC trace (a) and fitted envelopes (b) of the Tsunami pulse at a distance of ≈ 3 m from the fs oscillator.

The IAC trace in fig.(5.3 (a)) is also that of the Tsunami pulse at 3 meters from the laser output but the only difference here is that a 5 mm thick BK-7 glass plate was inserted into the beam path just after exiting the fs oscillator. Again there was no clear correlation between the results of the lower envelope parameters to that of the upper envelope in fig.(5.3 (b)). Table 5.1 summarizes the pulse parameters obtained from the upper envelopes in figs.(5.2) and (5.3). The upper envelopes were chosen because compared to the lower envelopes, they have larger signal to background ratios.

In principle, the linear chirp parameter need not be included as a fit pa-

(a)   (b)
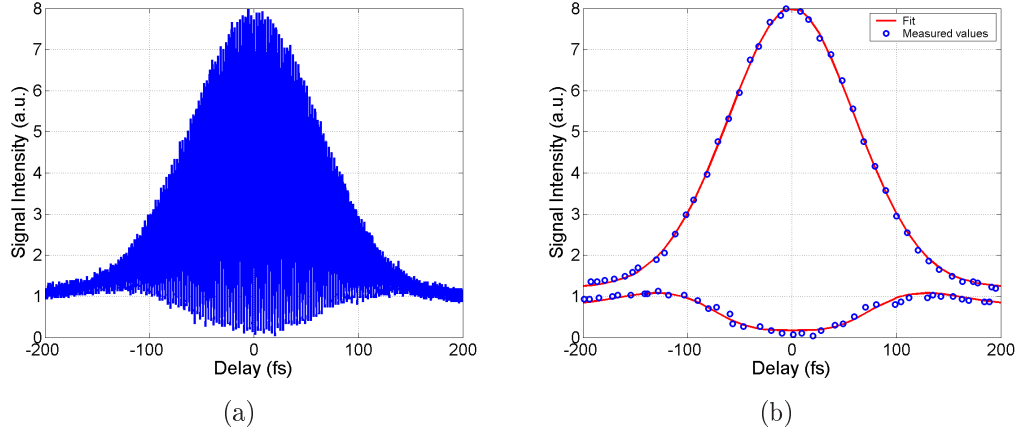
Figure 5.3: Measured IAC trace (a) and fitted envelopes (b) of the Tsunami pulse after passing through 5 mm BK-7 glass plate and also traveling a distance of ≈ 3 m from the fs oscillator.

	Pulse width $\Delta\tau$	Linear Chirp b_0	TBP $\Delta\nu\Delta\tau$
IAC trace from fig.(5.2)	123 ± 9.2 fs	1.88 ± 0.32	0.78
IAC trace from fig.(5.3)	141 ± 5.4 fs	2.03 ± 0.18	0.89

Table 5.1: Pulse parameters determined through IAC.

rameter, seeing that it could be determined using the TBP only[1]. Also, in routine pulse width monitoring the fit in eq.(5.1) is not explicitly used. A simpler method is to merely count the number of maxima's N above the half-maximum value of 4.5 in figs.(5.2 (a)) and (5.3 (a)), and multiplying it by the center wavelength over the speed of light, λ_0/c. This leads to the FWHM of the IAC trace $\Delta\tau_{IAC} = N\lambda_0/c$. The pulse width is then simply approximated as $\Delta\tau \approx \Delta\tau_{IAC}/\sqrt{2}$.

5.1.2 MOSAIC results

The experimentally obtained MOSAIC traces in figs.(5.4 (a)) and (5.5 (a)) both show a noticeable 'double-hump' structure on the bottom. As previously stated in section 3.2, the presence of this structure signifies that the pulse

---

[1]See eq.(2.30).
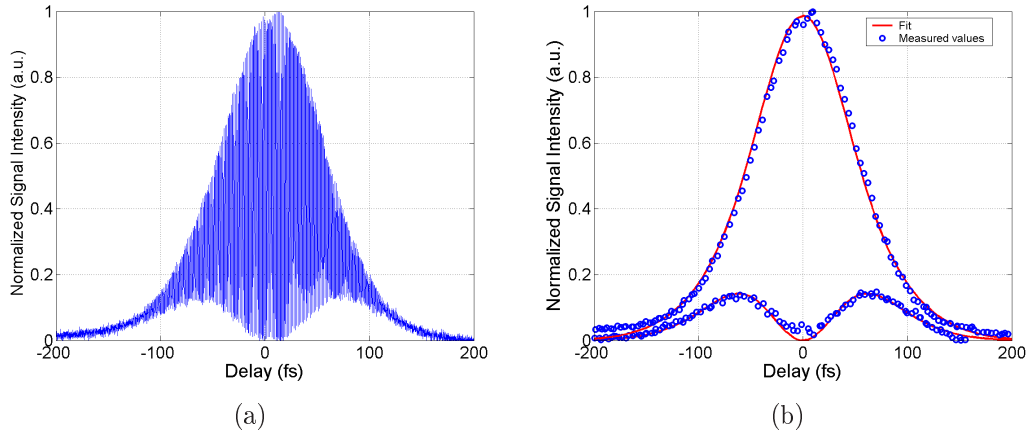
Figure 5.4: Measured MOSAIC trace (a) and fitted envelopes (b) for Tsunami pulse in fig.(5.2).

under investigation is chirped. For this reason, the amount of chirp on the pulse is determined by fitting the upper and lower envelopes of eq.(3.11) for a linearly chirped Gaussian pulse model to the traces in figs.(5.4 (a)) and (5.5 (a)). The equations used for fitting the upper and lower envelopes in
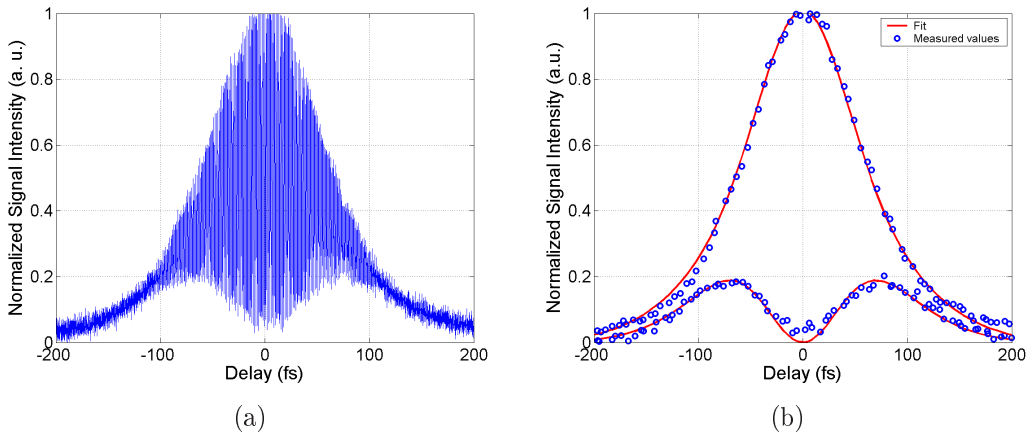

Figure 5.5: Measured MOSAIC trace (a) and fitted envelopes (b) for Tsunami pulse in fig.(5.3).

	Pulse width $\Delta\tau$	Linear Chirp b_0
MOSAIC trace from fig.(5.4):		
Upper Envelope	110.6 ± 2.4 fs	1.46 ± 0.12
Lower Envelope	103.7 ± 6.5 fs	1.64 ± 0.31
MOSAIC trace from fig.(5.5):		
Upper Envelope	134.3 ± 3.6 fs	1.74 ± 0.15
Lower Envelope	120.9 ± 11.1 fs	1.72 ± 0.46

Table 5.2: Pulse parameters determined through MOSAIC.

figs.(5.4 (b)) and (5.5 (b)) are;

$$
\begin{aligned}
G_{\pm}^{MOSAIC}(\tau) &= A_0^4 \left\{ \exp\left\{ -2\ln 2 \left(\tfrac{\tau}{\Delta\tau}\right)^2 \right\} \right. \\
&\pm \left. \exp\left\{ -2\ln 2 \left[1 + b_0^2\right] \left(\tfrac{\tau}{\Delta\tau}\right)^2 \right\} \right\}
\end{aligned}
\tag{5.2}
$$

where '$+$' denotes the upper and '$-$' the lower envelopes of the normalized MOSAIC trace. Seeing that $\Delta\tau$ is also present in eq.(5.2), MOSAIC is also capable of determining the pulse width. The fitting parameters in eq.(5.2) for figs.(5.4 (b)) and (5.5 (b)) are summarized in table 5.2.

5.1.3 BFA results

Fig.(5.6) shows the BFA trace of the Tsunami pulse measured at a distance of 3 meters from the laser output. The fit function used in fig.(5.6), is the theoretically calculated BFA trace for a Gaussian pulse from eq.(3.13). This fit allows for the extraction of pulse width information only. An attempt

Pulse Shape:	Pulse width $\Delta\tau$
Gaussian	91.99 ± 0.20 fs
Sech	81.64 ± 0.23 fs
Lorentzian	61.67 ± 0.52 fs
Two-sided exponential	57.13 ± 0.32 fs

Table 5.3: Pulse width determined through BFA.

was also made to fit BFA traces of different pulse shapes. The shapes used
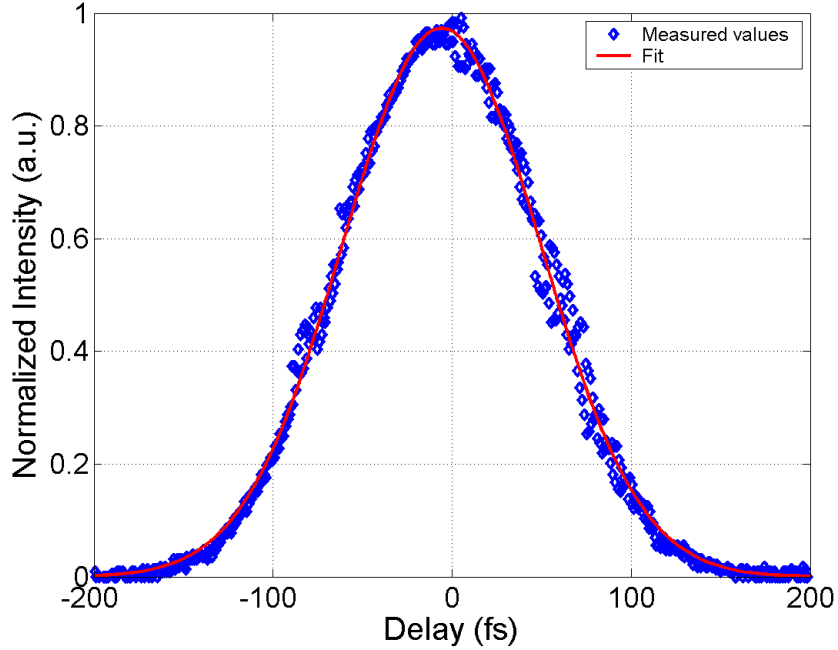
Figure 5.6: Measured BFA trace for the Tsunami pulse fitted with a Gaussian pulse model.

includes the Sech-pulse, the Lorentzian pulse and a two-sided exponential pulse. Pulse width determination of these pulses were done through fitting the respective BFA models in table 3.1 to the experimental data in fig.(5.6). These results, as well as the result of the fit in fig.(5.6) are summarized in table 5.3.

5.1.4 SHG FROG results

Fig.(5.7 (a)) shows the experimentally obtained SHG FROG trace for the Tsunami pulse using the setup shown in fig.(4.9). This measured trace was then used as input trace for the FROG algorithm software resulting in the reconstructed trace in fig.(5.7 (b)). The FROG algorithm uses a square grid of wavelength (or frequency) versus delay values to sample data from the measured FROG trace. The grid size chosen for the trace in fig.(5.7 (a)) was 256×256. Choosing the correct grid size such that the entire trace

data is covered, is paramount in satisfying the Nyquist sampling rate limit. Using this grid size a reconstructed FROG trace was generated with only 186 iterations in less than one minute.
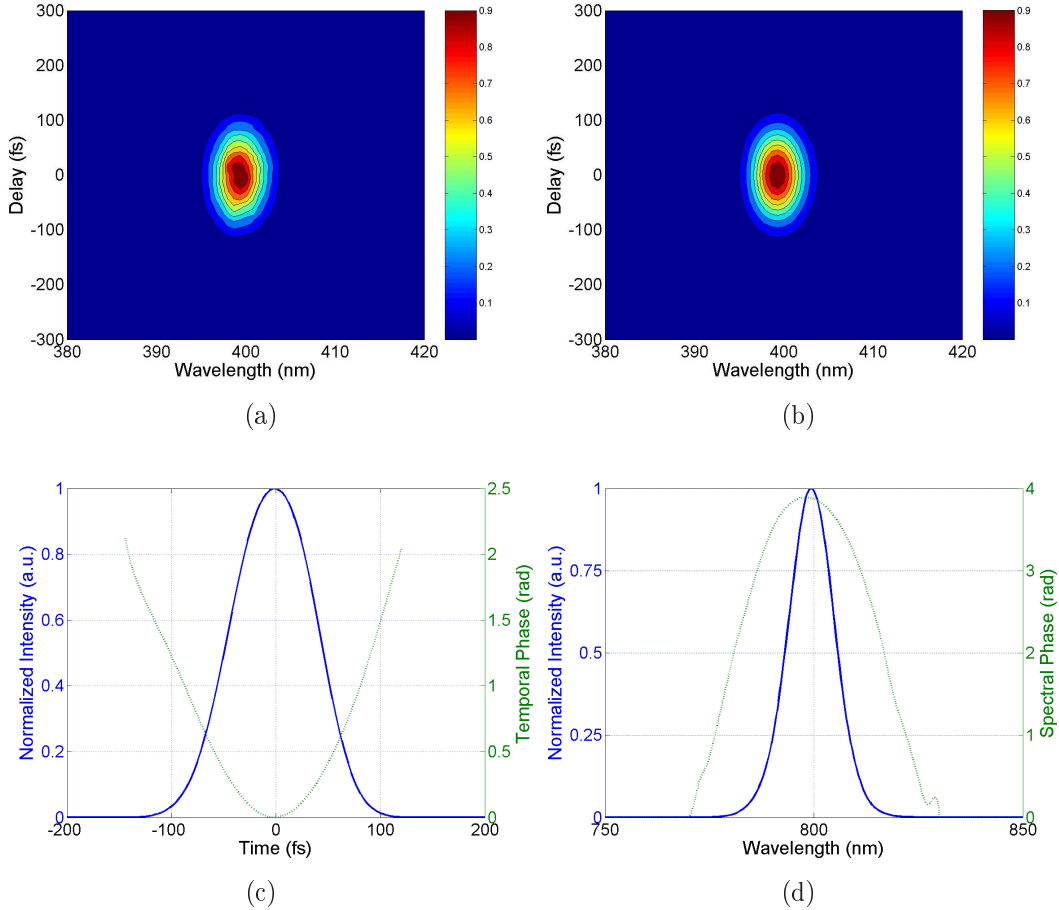
Figure 5.7: SHG FROG of the Tsunami pulse; (a) Measured FROG trace, (b) Reconstructed FROG trace, (c) Retrieved Temporal Intensity (solid line) and phase (dashed line), (d) Retrieved Spectral Intensity (solid line) and spectral phase (dashed line).

The temporal and spectral intensities together with their relative phases, which are used for the reconstructed trace in fig.(5.7 (b)), are shown in figs.(5.7 (c)) and (5.7 (d)). The retrieved temporal intensity has a FWHM of 94.62 fs, whilst the spectral intensity has a FWHM of 12.56 nm. This means that the TBP of the retrieved pulse is 0.56.

5.2 Characterization of the Amplified pulse

5.2.1 BFA results

Fig.(5.8) shows the BFA measurement for the amplified Tsunami pulse measured a distance of 2 meters from the amplifier output. As was done for the Tsunami pulse, different pulse shapes were fitted to the measured BFA trace in fig.(5.8), with the results thereof summarized in table 5.4.
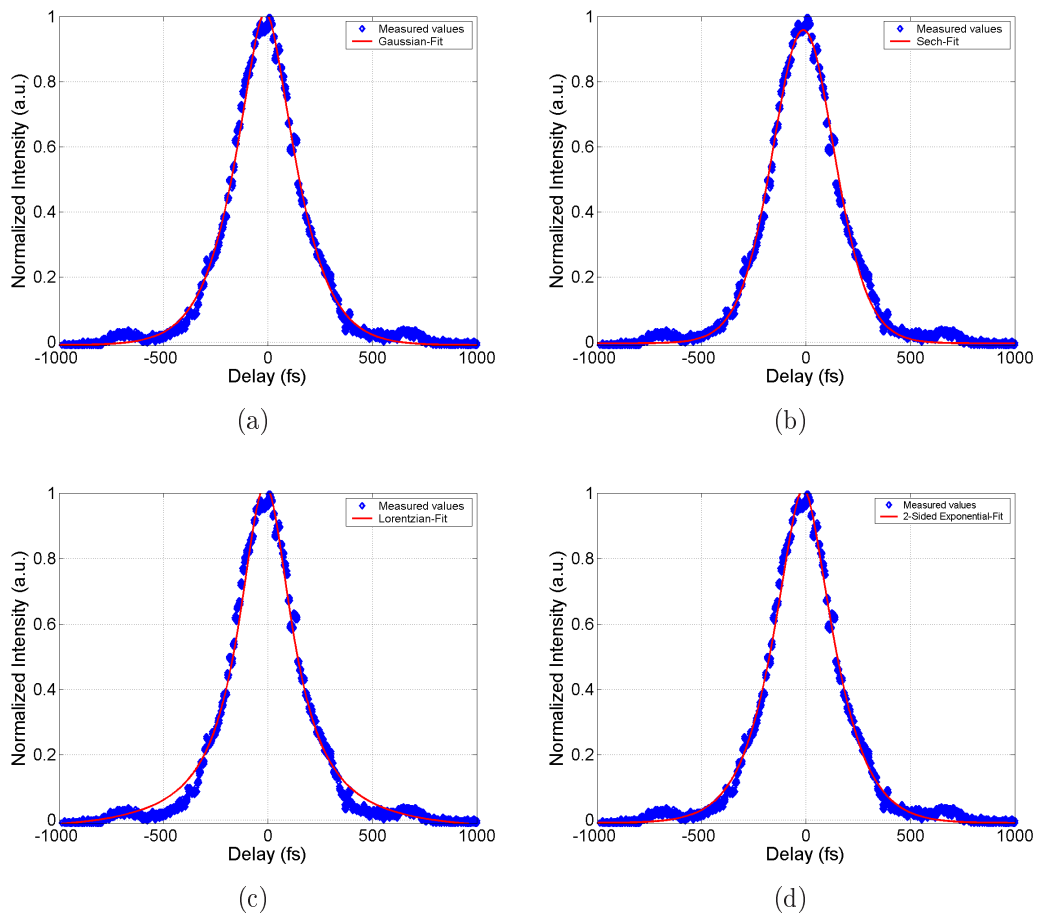
Figure 5.8: Measured BFA trace for the Amplified pulse fitted with; (a) a Gaussian pulse model, (b) a sech pulse model, (c) a Lorentzian pulse model and (d) a two-sided exponential pulse.

It should be noted that the measured trace in fig.(5.8) has secondary peaks

at delay times of approximately -700 and $+700$ fs. The presence of these peaks becomes more apparent when replotting fig.(5.8) in terms of the log of the normalized intensity versus delay time, as depicted in fig.(5.9). It is clear from fig.(5.9) that the intensity of the main peak (at 0 fs) is at least three orders of magnitude greater then the intensities of the secondary peaks (at ±700 fs).

Pulse Shape:	Pulse width $\Delta\tau$
Gaussian	258.60 ± 0.90 fs
Sech	227.90 ± 0.70 fs
Lorentzian	157.30 ± 0.85 fs
Two-sided exponential	157.80 ± 0.50 fs

Table 5.4: Pulse width of the amplified pulse determined through BFA.
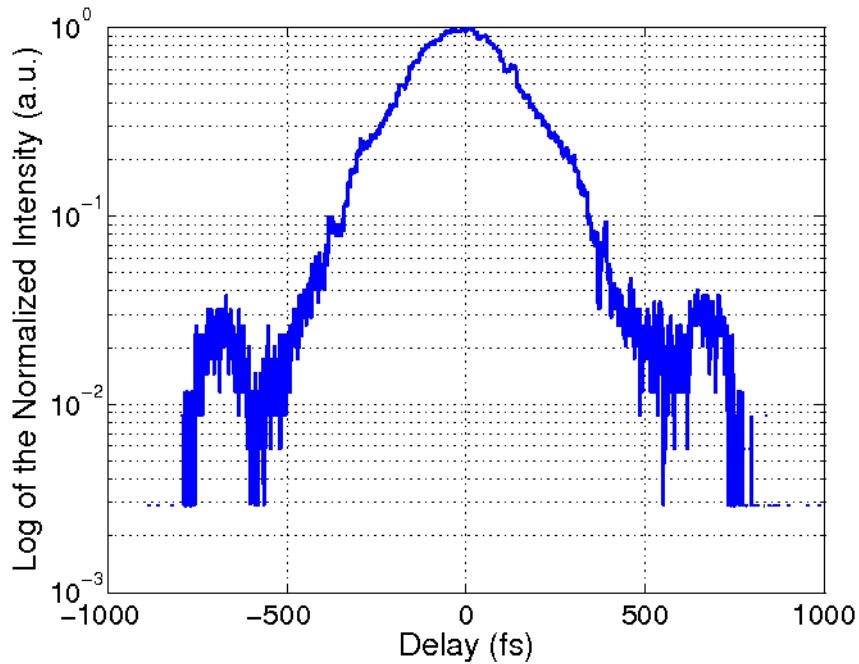
Figure 5.9: Log of the normalized intensity versus delay time for the measured BFA trace in fig.(5.8).

5.2.2 SHG FROG results

Fig.(5.10) shows the measured FROG trace together with the reconstructed pulse characteristics of a somewhat compressed amplified pulse with $\Delta\tau = 169.02$ fs, $\Delta\lambda = 10.40$ nm and TBP $= 0.82$. The algorithm reached this result after 299 iterations in about two minutes. A grid size of 256×256 was
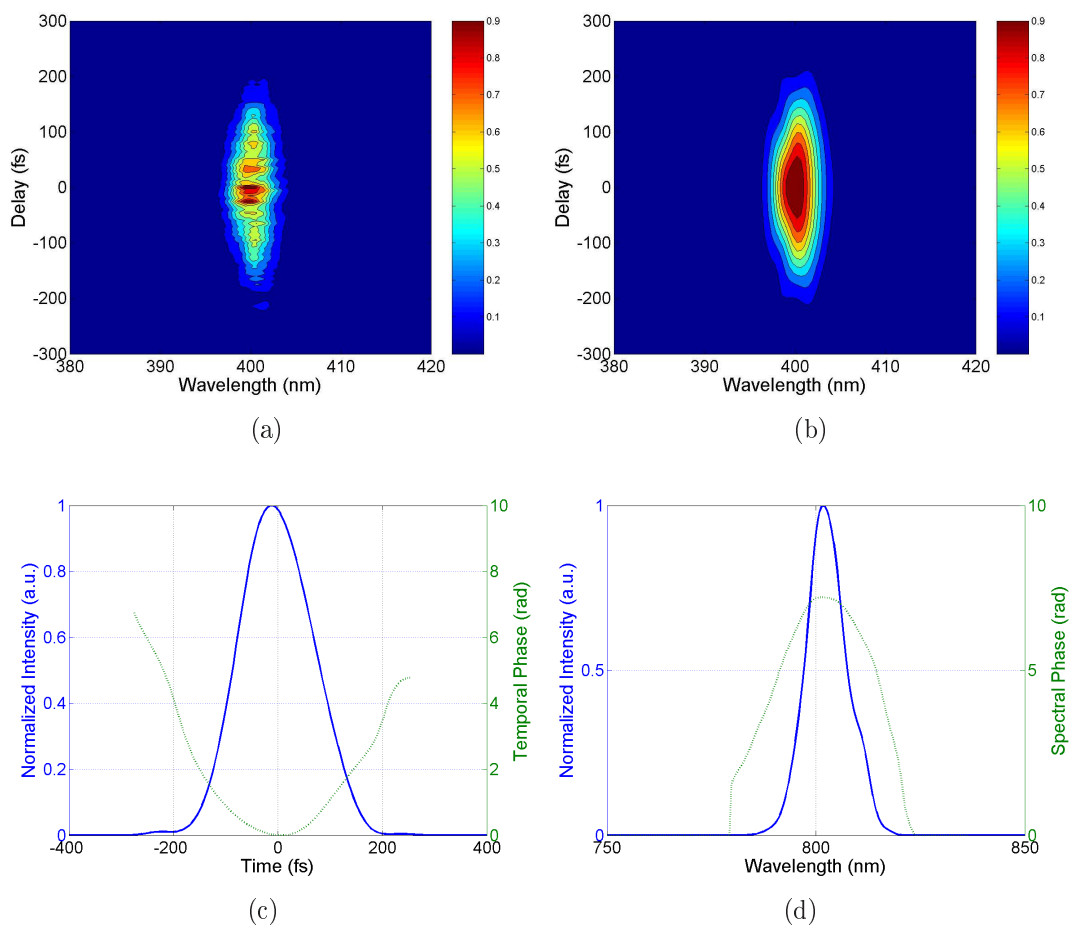
Figure 5.10: SHG FROG of the Alpha-1000 S amplifier system when compression is nearly optimal. (a) Measured FROG trace, (b) Reconstructed FROG trace, (c) Retrieved Temporal Intensity (solid line) and phase (dashed line), (d) Retrieved Spectral Intensity (solid line) and spectral phase (dashed line).

chosen to analyze the trace in fig.(5.10). A FROG trace was also recorded for

an uncompressed amplified pulse (fig.(5.11 (a))). The reason for calling the trace in fig.(5.11) uncompressed, is because the retrieved temporal intensity in fig.(5.11 (c)) is clearly broader then the intensity in fig.(5.10 (c)).

(a)

(b)

(c)

(d)
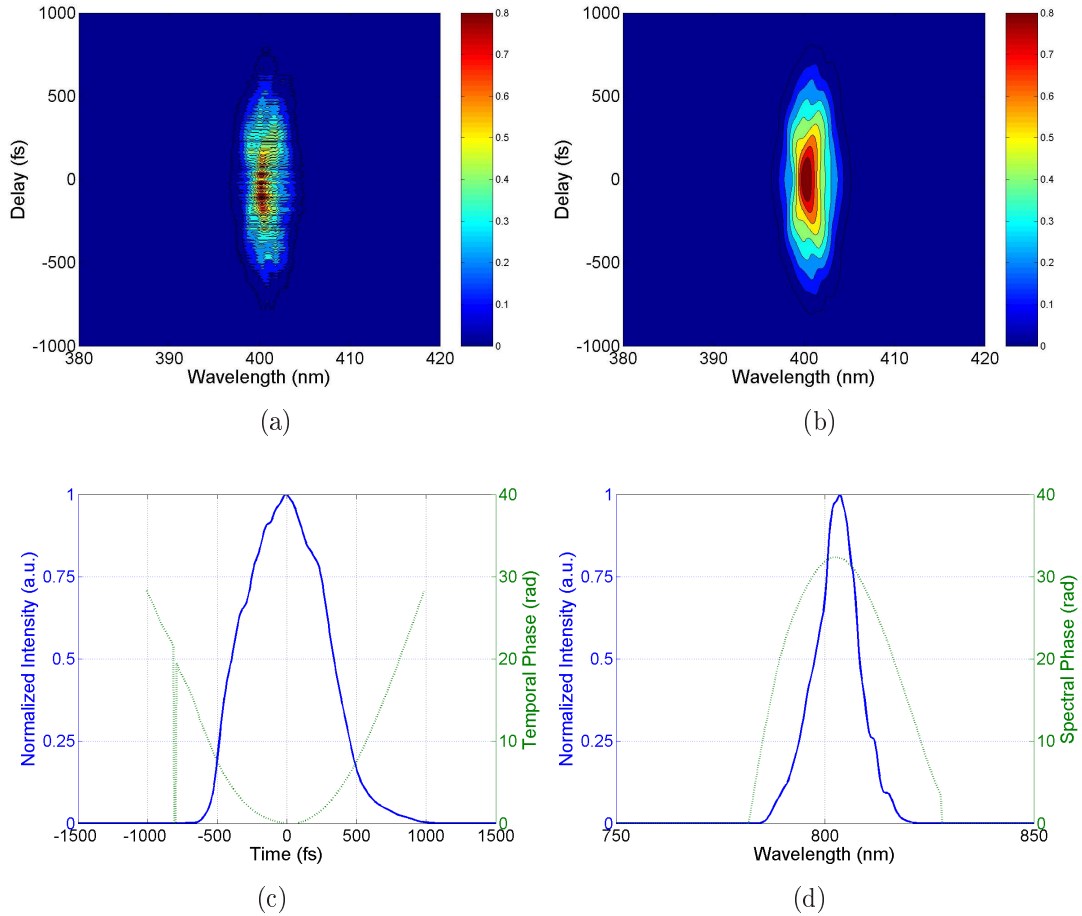
Figure 5.11: SHG FROG of the Alpha-1000 S amplifier system when compression is not optimal. (a) Measured FROG trace, (b) Reconstructed FROG trace, (c) Retrieved Temporal Intensity (solid line) and phase (dashed line), (d) Retrieved Spectral Intensity (solid line) and spectral phase (dashed line).

A 1024×1024 grid was selected, which proved to be sufficient in reconstructing the entire FROG trace. The reconstruction took almost ten minutes with the algorithm reaching a suitable retrieved trace after 576 iterations. The pulse information extracted from figs.(5.11 (c)) and (5.11 (d)) are

$\Delta\tau = 734.21$ fs and $\Delta\lambda = 10.73$ nm. This means that the TBP for this pulse has the value of 3.68.

Chapter 6

Discussions

Pulse characterization through IAC was only done for pulses emitted by the fs oscillator. The reason for this is that the pulse repetition rate of the amplified system (20 Hz) is of the same order as the mirror oscillation ($0-50$ Hz) in the IAC setup fig.(4.5). Therefore IAC of the 20 Hz amplified pulse system would be impossible since data accumulation would be insufficient for forming an IAC trace.

The IAC results suggest that the Tsunami pulse width measured at a distance of 3 meters from the laser output is significantly chirped. This is evident from the TBP being greater than the value of 0.441 for a bandwidth-limited Gaussian pulse. The presence of chirp on the laser pulse is attributed mainly to dispersion. The pulse moves through a dispersive medium, it experiences substantial GVD and as a result is temporally broadened. The dispersive elements in the beam path include an energy attenuator, air and of course the beam splitter used in the IAC setup itself. The attenuator is used to attenuate the pulse energy such that the measured IAC trace is recorded in a region where the non-linear detector in fig.(4.5) works optimally. This attenuator consists of a polarizer and half wave plate, which is normally made of quartz (SiO_2) or calcite ($CaCO_3$) crystals. As an example, the GVD at 800 nm for an ordinary wave traveling through calcite is calculated to be 720 fs^2/cm [33]. This means that an unchirped pulse with an initial FWHM of 80 fs traveling through a 2 cm thick calcite crystal at ordinary polarization, will

be broadened to about 94 fs according to eq.(2.68). The initial FWHM of 80 fs is chosen, because according to the Tsunami specifications, this is what is to be expected for a pulse with a center wavelength of 800 nm [28]. The thickness of the calcite crystal chosen matches the experimental conditions. The expected pulse width of 94 fs falls outside the 95% confidence bounds for the measured FWHM in row one of table 5.1. However, assuming that the pulse has an initial normalized chirp value of $b_0 = 0.65$ the expected pulse width increases to 123 fs, which matches the measured value exactly. Assuming that the pulse has an initial chirp is acceptable because it moves through a grating pair and the output coupler before exiting the laser cavity as described in section (4.1).

The measured IAC trace for the pulse which travels through an additional 5 mm thick BK7 glass is not expected to vary as significantly as the results in table 5.1 suggest. This is because the the dispersion length through the BK7 glass medium is only 5 mm, which is insufficient to result in extreme pulse broadening even though the GVD at 800 nm is about 446 fs^2/cm [34]. This is supported by the calculation of a pulse width of 126 fs, for the pulse which traveled through both the calcite crystal and the BK7 glass. Nevertheless, from the result in the second row of table 5.1 it seems as if the addition of the BK7 glass plate increases the total GVD such that a pulse which is temporally broader than expected is measured. Incidentally, temporal pulse broadening resulting from air dispersion is also a source of additional broadening, but this is neglected because the GVD of air is only 0.21 fs^2/cm, which is considerably smaller then that of the BK7 glass and the calcite crystal [35].

The MOSAIC results for the Tsunami pulse mirror the results obtained through IAC. The true value of the MOSAIC technique to measure extremely small chirp values was not explicitly evident. However, what is evident from the results in table 5.2, is the effect the insertion of the 5 mm BK7 glass plate has on the pulse width and linear chirp parameter. It should be noted that the reconstructed MOSAIC traces were generated using software which also allows for MOSAIC reconstruction over a number of IAC traces[1]. In

---

[1]This software is available from http://www.optics.unm.edu/sbahae.

recent times it has been shown that when the MOSAIC trace is generated from averaging over a number of IAC traces, exact chirp measurements with signals close to the noise level and non-quadratic detectors are possible [36]. What is even more impressive is that full-field reconstruction of ultrashort pulses is now also possible with MOSAIC. Bender et al. showed that when the IAC and SHG spectral data of a pulse are captured simultaneously, a MOSAIC trace can be reconstructed which is sensitive to both temporal and spectral phase changes [37].

The BFA results of the various pulse shapes for the Tsunami pulse in table 5.3 differ significantly. The question remains, which value in table 5.3 correctly describes the pulse width? The intuitive answer is, the value with the smallest fitting error. This minimum error requirement merely implies that the correctly extracted pulse width results from the model which fits the measured data the best. In this regard, the Gaussian pulse model fitted, having the smallest fitting error, fits the BFA trace the best. Keeping this minimum error idea in mind, the Gaussian model on the other hand, is not the best fit for the BFA trace of the amplified pulse as seen in table 5.4. Therefore, the two-sided exponential model is favoured due to the smaller error value.

Another interesting result from the BFA measurement of the amplified pulse, are the secondary peaks at ± 700 fs in fig.(5.4). These peaks suggest that the input pulse is actually a double pulse. This is easily verified when assuming a double pulse with separation time τ_{sep} and intensity profile $I(t) = I_0(t) + I_0(t + \tau_{sep})$ and then calculating the BFA trace from eq.(3.12);

$$G_{BFA}^{(2)}(\tau) = G_0^{(2)}(\tau + \tau_{sep}) + 2G_0^{(2)}(\tau) + G_0^{(2)}(\tau - \tau_{sep}) \qquad (6.1)$$

where $G_0^{(2)}(\tau) = \int_{-\infty}^{\infty} I_0(t-\tau)I_0(t)dt$. It is clear from eq.(6.1) that the secondary peaks at $\pm\tau_{sep}$ appear in the BFA trace for a double pulse. This means that the amplified pulse truly is a double pulse, with the two pulses separated by 700 fs. The only limitation due to the ambiguity of the BFA trace, is that it is impossible to determine time direction and thus whether the second pulse from fig.(5.8) leads or trails the main pulse.
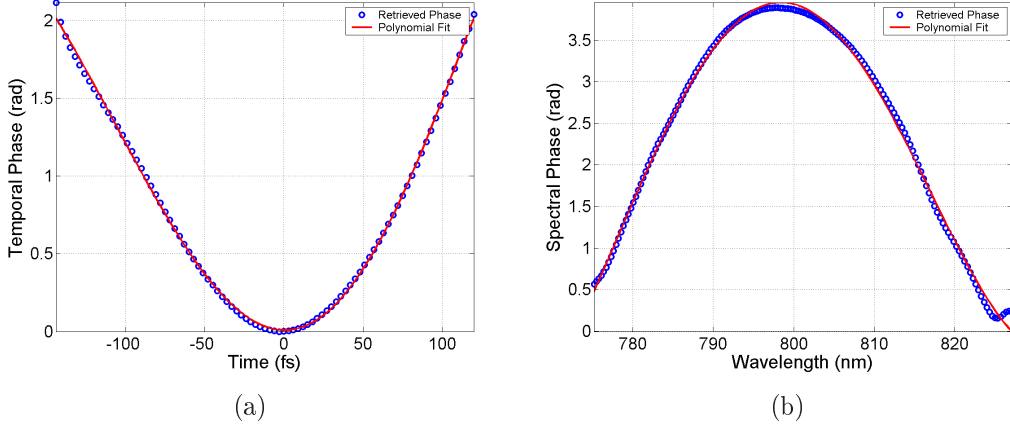
Figure 6.1: Temporal (a) and spectral (b) phase of the Tsunami pulse.

The FROG results of both the Tsunami and amplified pulses, show how powerful this technique is in full-field reconstruction. Besides the retrieval of the various pulse widths and intensities, the FROG results also include temporal and spectral phase information. It is clear from figs.(5.7 (c)-(d)), (5.10 (c)-(d)) and (5.11 (c)-(d)) that the retrieved temporal and spectral phases have definite structure. In order to examine this structure, a higher order polynomial fit is applied to both the temporal and spectral phase of fig.(6.1 (a) & (b)) and plotted in fig.(5.7 (c) & (d)) respectively. The polynomial fit for the temporal phase is:

$$\phi(t) = \phi_0 + \phi_1\frac{t}{\Delta\tau} + \phi_2\left(\frac{t}{\Delta\tau}\right)^2 + \phi_3\left(\frac{t}{\Delta\tau}\right)^3 + \phi_4\left(\frac{t}{\Delta\tau}\right)^4 + \phi_5\left(\frac{t}{\Delta\tau}\right)^5 \quad (6.2)$$

with ϕ_0, ϕ_1, ϕ_2, ϕ_3, ϕ_4 and ϕ_5 being the fitting parameters. This temporal phase fit is chosen such that the fitting parameters are normalized to the pulse width $\Delta\tau$. The fit used for the spectral phase is similar to the one in eq.(6.2),

$$\varphi(\lambda) = \varphi_0 + \varphi_1 \times (\lambda - \lambda_0) + \varphi_2 \times (\lambda - \lambda_0)^2 + \varphi_3 \times (\lambda - \lambda_0)^3 + \varphi_4 \times (\lambda - \lambda_0)^4 \quad (6.3)$$

where φ_0, φ_1, φ_2, φ_3, φ_4 and λ_0 are the fitting parameters. Table 6.1 summarizes the fitting parameters in eq.(6.2) for the temporal phases in figs.(5.7

	Phase from fig.(5.7 (c))	Phase from fig.(5.10 (c))	Phase from fig.(5.11 (c))
ϕ_0 (rad)	14.76×10^{-3}	62.61×10^{-4}	-23.22×10^{-2}
ϕ_1 (rad/fs)	-15.26×10^{-5}	-62.79×10^{-3}	-52.78×10^{-2}
ϕ_2 (rad/fs^2)	1.353	2.818	17.64
ϕ_3 (rad/fs^3)	0.1196	0.8249	1.238
ϕ_4 (rad/fs^4)	-0.1395	-0.2317	-1.099
ϕ_5 (rad/fs^5)	-32.43×10^{-4}	-0.8277	-0.4465

Table 6.1: Temporal phase fitting parameters.

(c)), (5.10 (c)) and (5.11 (c)). What is apparent from table 6.1, is that the quadratic contribution in all cases is the greatest. This implies that the three investigated pulses are mostly linearly chirped. More specifically, the pulses are all positively chirped. The third- and higher-order terms of the temporal phase in eq.(6.2) are generally not considered. Higher-order phase distortions are rather examined in the frequency or wavelength domain, because a pulse's spectrum is more easily measured than its temporal intensity. Thus, the determination of the spectral phase in general yields the complete pulse field.

	Phase from fig.(5.7 (d))	Phase from fig.(5.10 (d))	Phase from fig.(5.11 (d))
φ_0 (rad)	3.574	7.032	29.05
φ_1 (rad/nm)	0.1082	0.1354	0.9147
φ_2 (rad/nm^2)	-72.74×10^{-4}	-20.10×10^{-3}	-62.76×10^{-3}
φ_3 (rad/nm^3)	-84.06×10^{-6}	28.76×10^{-6}	-57.64×10^{-5}
φ_4 (rad/nm^4)	34.78×10^{-7}	98.49×10^{-7}	15.30×10^{-6}
λ_0 (nm)	791.5	798.4	795.6

Table 6.2: Spectral phase fitting parameters.

Finally, it should be mentioned that the spectral phase fitting parameters summarized in table 6.2, can furthermore be used to study non-linear pulse propagation through dispersive media [38].

Chapter 7

Conclusions

The purpose of the presented work was to develop techniques and the apparatus to characterize ultrashort laser pulses emitted by a commercially available fs oscillator and a regenerative amplifier. The difference in dynamics between the two laser systems, prompted the use of pulse characterization techniques capable of measuring optical pulse durations in the order of fs up to ps. Four techniques namely, IAC, MOSAIC, BFA and SHG FROG were used for pulse characterization. The latter two experimental setups were designed and constructed especially for this work.

IAC as well as MOSAIC showed that the pulse emitted by the Tsunami laser has a pulse width in the vicinity of $103 - 123$ fs with a linear chirp parameter around $1.4 - 1.8$, when measured after passing through an attenuator and propagating for 3 meters through air. The effect of introducing additional GVD was also studied through the insertion of a 5 mm BK7 glass plate into the beam path. It was found that the pulse width increased to values in the region of $120-141$ fs with the linear chirp parameter also increasing to values around $1.7-2.0$. This implies that the insertion of a 5 mm thick transparent BK7 glass plate into the beam path causes temporal pulse broadening of up to 10 fs.

The constructed BFA setup was used to measure the pulse widths of pulses emitted by both the fs oscillator and a regenerative amplifier. It was shown

that correct pulse width extraction can only be deduced using the model to best fit the BFA results. For pulse width extraction of the Tsunami pulse, a Gaussian model was used which rendered a pulse width of 92 fs. A two-sided exponential model seemed to fit the BFA trace of the amplified pulse the best. This resulted in a measured pulse width of about 158 fs. An interesting observation was also made from the BFA trace of the amplified pulse. The BFA trace consisted of three distinct peaks, a main peak at zero delay time ($\tau = 0$), a peak at $\tau = -700$ fs and also one at $\tau = 700$ fs. It was concluded that the presence of the two secondary peaks at delays times $\tau = \pm 700$ fs suggests that the amplified pulse actually has a double pulse structure with the two pulses separated by 700 fs.

Pulse characterization through SHG FROG was done for both the Tsunami laser pulse as well as the amplified pulse. Of all the techniques used in this work, FROG proved to be the one capable of full field reconstruction. Three different pulses were characterized using FROG. The first was a pulse directly from the fs oscillator, whilst the other two were amplified pulses of different pulse durations. What was clear from the retrieved temporal and spectral phases for the different pulses, was that they all posses positive linear chirp. A pulse width of 95 fs was recorded for the Tsunami pulse, whereas pulse widths of 170 fs and 734 fs were measured for the amplified pulse when compression was nearly optimal and not optimal, respectively.

In conclusion, successful construction and characterization of different pulse characterization techniques applied during the course of this work all serve their own unique purposes. IAC is ideal for routine pulse width measurement and linear chirp determination of high repetition rate (kHz-MHz) fs pulses. The same applies of course to MOSAIC. BFA on the other hand is perfect for slow and complete temporal characterization of ultrashort laser pulses. Due to the time consuming aspect of SHG FROG, it is not generally used for routine pulse characterization. Therefore, it is rather only used when complete characterization is required. However, if routine monitoring of pulse duration is required, IAC and even BFA is preferred.

Bibliography

[1] T. H. Maiman. Stimulated optical radiation in ruby. *Nature*, 187(4736):493–494, August 1960.

[2] P. A. Franken, A. E. Hill, C. W. Peters, and G. Weinreich. Generation of optical harmonics. *Phys. Rev. Lett.*, 7(4):118–119, Aug 1961.

[3] L. E. Hargrove, R. L. Fork, and M. A. Pollack. Locking of He-Ne laser modes induced by synchronous intracavity modulation. *Applied Physics Letters*, 5(1):4–5, 1964.

[4] D. von der Linde. Experimental study of single picosecond light pulses. *IEEE Journal of Quantum Electronics*, 8(3):328–338, March 1972.

[5] D. Kuizenga. Generation of short pulses for laser fusion in an actively mode-locked Nd:YAG laser. *IEEE Journal of Quantum Electronics*, 13(9):878–879, September 1977.

[6] R. L. Fork, B. I. Greene, and C. V. Shank. Generation of optical pulses shorter than 0.1 psec by colliding pulse mode locking, 1981.

[7] P. F. Moulton. Spectroscopic and laser characteristics of ti:sapphire., 1986.

[8] P. Maine, D. Strickland, P. Bado, M. Pessot, and G. Mourou. Generation of ultrahigh peak power pulses by chirped pulse amplification. *IEEE Journal Of Quantum Electronics*, 24(2):398–403, February 1988.

[9] S. H. Cho, U. Morgner, and F. X. Kärtner. Sub-two-cycle pulses from a kerr-lens mode-locked Ti:Sapphire laser. *Optics Letters*, 24(6):411, 1999.

[10] V. Scheuer, R. Ell, Fujimoto, and J. G. Generation of 5-fs pulses and octavespanning spectra directly from a Ti:Sapphire laser. *Optics Letters*, 26(6):373, 2001.

[11] D. Meshulach, Y. Barad, and Y. Silberberg. Measurement of ultrashort optical pulses by third-harmonic generation. *Journal Of The Optical Society Of America B-Optical Physics*, 14(8):2122–2125, August 1997.

[12] C. Iaconis and I. A. Walmsley. Spectral phase interferometry for direct electric-field reconstruction of ultrashort optical pulses. *Optics Letters*, 23(10):792–794, May 1998.

[13] A. Baltuska, M. S. Pshenichnikov, and D. A. Wiersma. Amplitude and phase characterization of 4.5-fs pulses by frequency-resolved optical gating. *Optics Letters*, 23(18):1474–1476, September 1998.

[14] T. Hirayama and M. Sheik-Bahae. Real-time chirp diagnostic for ultrashort laser pulses. *Optics Letters*, 27(10):860–862, May 2002.

[15] D. J. Bottomley, G. Lupke, C. Meyer, and Y. Makita. Exact separation of surface and bulk contributions to anisotropic 2nd-harmonic generation from cubic centrosymmetric media. *Optics Letters*, 20(5):453–455, March 1995.

[16] D. J. Bottomley, A. Mito, S. Niki, and A. Yamada. Second-harmonic generation from chalcopyrite-structure semiconductor thin films. *Optics Letters*, 21(4):254–256, February 1996.

[17] Torsten Scheidt. *Charge Carrier Dynamics And Defect Generation At The Si/SiO Probed By Femtosecond Optical Second Harmonic Generation*. PhD thesis, Physikalisch-Astronomische Fakultät Friedrich-Schiller-Universität Jena, 2005.

[18] J. Boudeile, F. Druon, M. Hanna, P. Georges, Y. Zaouter, E. Cormier, J. Petit, P. Goldner, and B. Viana. Continuous-wave and femtosecond laser operation of Yb:CaGdAlO$_4$ under high-power diode pumping. *Optics Letters*, 32(14):1962–1964, July 2007.

[19] J. Saikawa, Y. Sato, T. Taira, and A. Ikesue. Femtosecond Yb:YSAG ceramic laser. *Optical Materials*, 29(10):1283–1288, June 2007.

[20] Jean-Claude Diels and Wolfgang Rudolph. *Ultrashort Laser Pulses Phenomena; Fundamentals, Techniques, and Applications on a Femtosecond time scale.* Academic Press, 1996.

[21] S. V. Popruzhenko, N. I. Shvetsov-Shilovski, S. P. Goreslavski, W. Becker, and G. G. Paulus. Two-dimensional streaking: complete characterization of an arbitrarily polarized few-cycle laser pulse using a stereodetector technique. *Optics Letters*, 32(11):1372–1374, June 2007.

[22] Eugene Hecht and Alfred Zajac. *Optics.* Addison-Wesley, Menlo Park, California, 1979.

[23] J. D. Jackson. *Classical Electrodynamics.* John Wiley & Sons, 1998.

[24] Amnon Yariv and Pochi Yeh. *Optical Waves in Crystals.* John Wiley and Sons, 2003.

[25] Robert W. Boyd. *Nonlinear Optics.* Academic Press, 2003.

[26] Peter Vasil'ev. *Ultrafast Diode Lasers: Fundamentals and Applications.* Artech House Publishers, 1995.

[27] Spectra-Physics. *Millennia Vs Diode-pumped, cw Visible Laser User's Manual*, 2001.

[28] Spectra-Physics. *Tsunami Mode-locked Ti:Sapphire Laser User's Manual*, 1999.

[29] Peter W Milonni and Joseph H Eberley. *Lasers.* John Wiley and Sons, 1988.

[30] B.M. Industries. *Short Pulse - High Repetition Rate System Alpha-1000 S User's Manual.*

[31] Continuum. *Powerlite 8000 Series Laser User's Manual*, 1993.

[32] R S Adhav, S R Adhav, and J M Pelaprat. BBO's nonlinear optical phase-matching properties. *Laser Focus Electro-Optics*, 23:88–101, 1987.

[33] V. Kartazaev and R. R. Alfano. Supercontinuum generated in calcite with chirped femtosecond pulses. *Optics Letters*, 32(22):3293–3295, 2007.

[34] J. K. Ranka, R. W. Schirmer, and A. L. Gaeta. Observation of pulse splitting in nonlinear dispersive media. *Physical Review Letters*, 77(18):3783–3786, October 1996.

[35] I. Alexeev, A. Ting, D. F. Gordon, E. Briscoe, J. R. Penano, R. F. Hubbard, and P. Sprangle. Longitudinal compression of short laser pulses in air. *Applied Physics Letters*, 84(20):4080–4082, May 2004.

[36] D. A. Bender, M. P. Hasselbeck, and M. Sheik-Bahae. Sensitive ultrashort pulse chirp measurement. *Optics Letters*, 31(1):122–124, January 2006.

[37] D. A. Bender and M. Sheik-Bahae. Modified spectrum autointerferometric correlation (MOSAIC) for single-shot pulse characterization. *Optics Letters*, 32(19):2822–28224, October 2007.

[38] H. K. Eaton, T. S. Clement, A. A. Zozulya, and S. A. Diddams. Investigating nonlinear femtosecond pulse propagation with frequency-resolved optical gating. *IEEE Journal Of Quantum Electronics*, 35(4):451–458, April 1999.